nature biomedical engineering

Article

https://doi.org/10.1038/s41551-026-01672-0

Polymer–mRNA complexes for monocyte-trafficked, lymph node-targeted cancer vaccination

Received: 3 March 2025

Accepted: 27 March 2026

Qiongzhe Ren[1,9], Xiaofei Zhao[1,9], Lili Zhou[2,9], Ruonan Ye[1], Liguo Chen[1], Keyun Ren[3], Xijun Piao[3], Yihan Zhou[4], Yiming Qi[5], Kevin C. Chan[4], Li Cao[6], Liang Du[7], Peng Gao[7], Bo Ying[7], Chao Deng[1], Fenghua Meng[1], Fangfang Zhou[2] ✉, Congcong Xu[1,6,8] ✉ & Zhiyuan Zhong[1,6,8] ✉

Lymph nodes are the primary sites where adaptive immunity is initiated, yet most messenger RNA cancer vaccines reach them inefficiently and instead accumulate in organs such as the liver, limiting therapeutic potency and increasing systemic toxicity. Here we developed a transferrin receptor-associating polyplex formed by electrostatic complexation of mRNA with low-molecular-weight polyethylenimine that had been chemically modified with cyclic disulfide monomers to enhance nucleic acid binding stability, enable thiol-based transferrin receptor engagement and reduce off-target liver uptake. After subcutaneous administration, these polyplexes activated innate immunity, rapidly recruited monocytes with high transferrin receptor expression and bound these cells through cyclic disulfide-mediated interactions. Monocytes then trafficked the vaccine to draining lymph nodes, where mRNA translation and antigen presentation occurred. Delivery of ovalbumin and interleukin 12 mRNA elicited strong antigen-specific cytotoxic T cell responses and inhibited melanoma progression and metastatic disease. Studies using Survivin and human papillomavirus antigens in distinct tumour models demonstrated broad applicability. This monocyte-driven lymph node-targeting strategy enables potent and selective delivery of mRNA cancer vaccines.

Messenger RNA technology has revolutionized the development of both prophylactic and therapeutic vaccines, offering broad applications against diseases like viral infections and cancers[1–4]. Despite recent clinical advancements, the vaccines available at present still suffer from suboptimal delivery to lymph nodes (LNs)—the primary sites of immune activation—and off-target accumulation in organs such as the liver, substantially reducing their efficacy and raising concerns over systemic toxicity[5–12]. Various strategies have been explored to address this challenge, including the development of novel lipid nanoparticle (LNP) formulations[13–15], exosome-based carriers[16,17], ionizable amphiphilic Janus dendrimers[18,19] and LNPs equipped with specific ligands[20,21]. However, these engineered delivery systems still exhibit a tendency to accumulate in non-lymphoid tissues and none of them have entered clinical evaluation. This underscores the urgent need for novel LN-specific messenger RNA-delivery approaches.

Transferrin receptor 1 (TfR1) plays a critical role in immune regulation[22,23] and is expressed at high levels on activated immune cells, including dendritic cells (DCs), monocytes and T cells[24–27]. Markedly higher levels of TfR1 expression have been previously observed in monocytes compared with other immune cells. Furthermore, the immunological roles of monocytes present a promising avenue for enhancing antitumor immunity[28–32]. Notably, monocytes are approximately

A full list of affiliations appears at the end of the paper. ✉e-mail: zhoufangfang@suda.edu.cn; xucc@suda.edu.cn; zyzhong@suda.edu.cn

20 times more abundant than DCs, a difference that is even more pronounced in humans compared with mice. Recent evidence underscores monocytes as a viable target for cancer vaccine development. Specifically, nano delivery approaches have improved monocyte targeting by decorating nanoparticles with mannose[33,34], galactose[35], CD163 (ref. 36) and apoptotic bodies[37]. Interestingly, phagocytic cells provide a fundamental line of defence in the bloodstream by indiscriminately capturing and eliminating circulating foreign substances. Their ability to recognise and remove particles across a broad spectrum of chemical and physical properties ensures robust systemic protection despite the lack of strict specificity. Given their capacity to efficiently transport antigens to LNs via high endothelial venules (HEV), leveraging the high expression of TfR1 on monocytes represents a feasible and innovative approach for achieving LN-specific targeting.

In this study we developed a polyethylenimine (PEI)-based transferrin receptor-associating polyplex, which we named TRAP, for LN-specific delivery of mRNA cancer vaccines (Supplementary Fig. 1). We demonstrate both theoretically and experimentally that dithiolane-modified TRAP enters cells by binding to TfR1 on the cell membrane, facilitating efficient mRNA expression in various cell types and outperforming the positive control Lipofectamine 2000. Following subcutaneous administration, we observed minimal mRNA expression in organs such as the liver, whereas mRNA expression in LNs was highly specific. Furthermore, we show that TRAP, through STING activation, recruits inflammatory monocytes to the injection site and cyclic disulfide groups anchored on the surface of TRAP–mRNA nanoparticles lead to strong adherence to Ly6C$^+$ monocytes, followed by migration to LNs. The targeted delivery of mRNA vaccines encoding tumour antigens and the cytokine interleukin (IL)-12 markedly enhanced LN-specific immune responses, activated CD8$^+$ T cells and effectively inhibited tumour progression in melanoma models. When combined with antibody to PD-1, the complete response rate in tumour models reached 60%. Moreover, vaccination with *Survivin* mRNA markedly prolonged the survival of B16F10 metastatic mice, highlighting the potential of the platform for durable and LN-targeted vaccine delivery through a monocyte-driven mechanism.

Results

Rational design of TRAP for TfR1 binding

TfR1 has been widely utilized as a target for therapeutic delivery, taking advantage of its highly differentiated expression profile and capacity of receptor-mediated endocytosis[27,38]. By analysing TfR1 expression across different immune-cell subsets (raw data collected from The Human Protein Atlas, https://www.proteinatlas.org/; accessed 7 August 2024) as shown in Fig. 1a, markedly elevated expression was observed in monocytes, highlighting its potential as a viable target for monocyte-mediated delivery. We then performed molecular dynamics simulations to elucidate the structural features of TfR1, revealing solvent-exposed Cys residues within the apical domain of its extracellular domain (Fig. 1b,c). Solvent-accessible surface area (SASA) analysis confirmed that these Cys residues are accessible for potential interactions. Compared with other membrane receptor proteins, TfR1 exhibits statistically significantly higher solvent accessibility for its Cys residues (Fig. 1d), highlighting its unique structural characteristics. Notably, under glycosylated conditions that more accurately mimic the physiological environment, the solvent exposure of these Cys residues was statistically significantly enhanced (Fig. 1e), suggesting more favourable conformations for ligand recognition. Furthermore, analyses of the ligand interactions revealed distinct binding patterns: the basal portion (composed of the protease-like and helical domains) binds transferrin[39], whereas the dimer interface region forms complexes with the hereditary hemochromatosis factor[40]. In contrast, the apical domain, which contains the exposed Cys residues, interacts with arenaviruses[41], the *Plasmodium vivax* invasion protein *Pv*RBP2b[42] and heavy-chain ferritin, thereby facilitating physiological access to the cell (Supplementary Fig. 2).

Previous studies suggested that the introduction of a disulfide moiety on self-assembled block co-polymer nanoparticle enhances the in vivo delivery efficiency of small molecules and protein drugs[43]. Low-molecular-weight PEI, which has a good safety profile as a result of faster clearance compared with its high-molecular-weight counterpart, could pose challenges in maintaining stable complexation with large mRNA molecules, especially during systemic circulation. Therefore, implementing other chemical modification on low-molecular-weight PEI to further stabilize mRNA complexation could promote its systemic delivery capability. The cyclic carbonate with a dithiolane structure 1,2-dithiolane trimethylene carbonate (DTC) was first synthesized and reported by our laboratory[44,45]. Here we synthesized a DTC-modified PEI (molecular weight, 1,800 Da) polymer (Fig. 1f and Supplementary Fig. 3a), TRAP. In respect that the surface Cys groups on monocyte membrane might facilitate cellular binding and uptake via disulfide group formation with TRAP, this design enables LN-selective mRNA delivery in vivo. This synthetic reaction was simple and efficient, and a series of TRAP polymers with different DTC grafting ratios could

Fig. 1 | Design and characterization of TRAP-mNV for enhanced cytosolic mRNA delivery. a, Transcript expression levels, calculated as normalized transcript per million (nTPM), in monocytes ($n = 5$ biological samples). PBMC, peripheral blood mononuclear cell. **b**, Schematic of TfR1 embedded in the membrane, highlighting the extracellularly exposed Cys residues. **c**, Representative molecular dynamics snapshot illustrating the solvent-accessible Cys residues in the apical domain of TfR1. **d**, SASA of Cys residues for different receptor proteins, calculated from independent molecular dynamics simulations ($n = 30$ independent simulations). **e**, SASA of Cys residues in molecular dynamics simulations of TfR1 with and without glycosylation ($n = 160$ independent simulations). **f**, Illustration of the fabrication process of TRAP-mNV. **g**, Hydrodynamic diameter and zeta potential of TRAP-mNV (left), together with a representative transmission electron microscopy image (right). **h**, Immunoprecipitation analysis of the binding between Flag–TfR1 and biotin-labelled TRAP. Immunoprecipitated proteins (top) and total protein expression levels in the whole-cell lysate (WCL; bottom) are shown. **i**, Schematic of the pathway for efficient cellular internalization mediated by TRAP–mRNA binding to TfR1. **j**, Representative three-dimensional reconstructed confocal microscopy images of DC2.4 cells after treatment with Cy5-labelled TRAP-mNV, the red chemical structure represents a five-membered cyclic disulfide structure. **k**, Immunoprecipitation analysis of the binding between Flag–TfR1 and biotin-labelled nTRAP or TRAP. **l**, Representative stimulated emission depletion microscopy images showing the intracellular localization of TRAP-mNV in DC2.4 cells. **m**, Pearson's correlation coefficients (PCC) for co-localization between TRAP-mNV and lysosomes ($n = 27$ biological samples; each dot represents one cell). **n**, Relative cellular uptake of TRAP-mNV in DC2.4 cells in the presence of various endocytosis inhibitors: amiloride hydrochloride (Ami), chlorpromazine hydrochloride (CPZ), dynasore, ferristatin II and DTNB. **o**, Relative cellular uptake of TRAP-mNV in DC2.4 cells pretreated with different concentrations of ferristatin II. **p**, Percentage of enhanced GFP (EGFP)$^+$ cells showing the expression levels of *EGFP* mRNA delivered by Lipofectamine 2000 (Lipo 2000) or TRAP to different cell lines (mRNA dose, 1 μg ml^{-1}). **n**–**p**, $n = 3$ biological samples per group. **a**,**m**, Data are presented as box-and-whisker plots, where the box represents the interquartile range (25th–75th percentiles), with the whiskers extending to the minimum and maximum values, the line in the box indicating the median and all individual data points displayed. **d**,**e**,**n**–**p**, Data are presented as the mean ± s.d. Statistical significance was determined using a one-way analysis of variance (ANOVA, two-sided; **d**,**n**,**o**), two-sided unpaired Student's *t*-test (**e**) or multiple two-sided unpaired Student's *t*-tests with correction for multiple comparisons (**p**); exact *P* values are provided; NS, not significant. **g**,**h**,**j**–**l**, The experiments were independently repeated at least three times with similar results. IB, immunoblotting; IP, immunoprecipitation; MW, molecular weight; Strep, strep-tactin; TF, transferrin. Panels created in BioRender: **f**, Ren, Q. https://biorender.com/6dck7ys (2026); **i**, Ren, Q. https://biorender.com/y8es8cs (2026). Source data are provided.

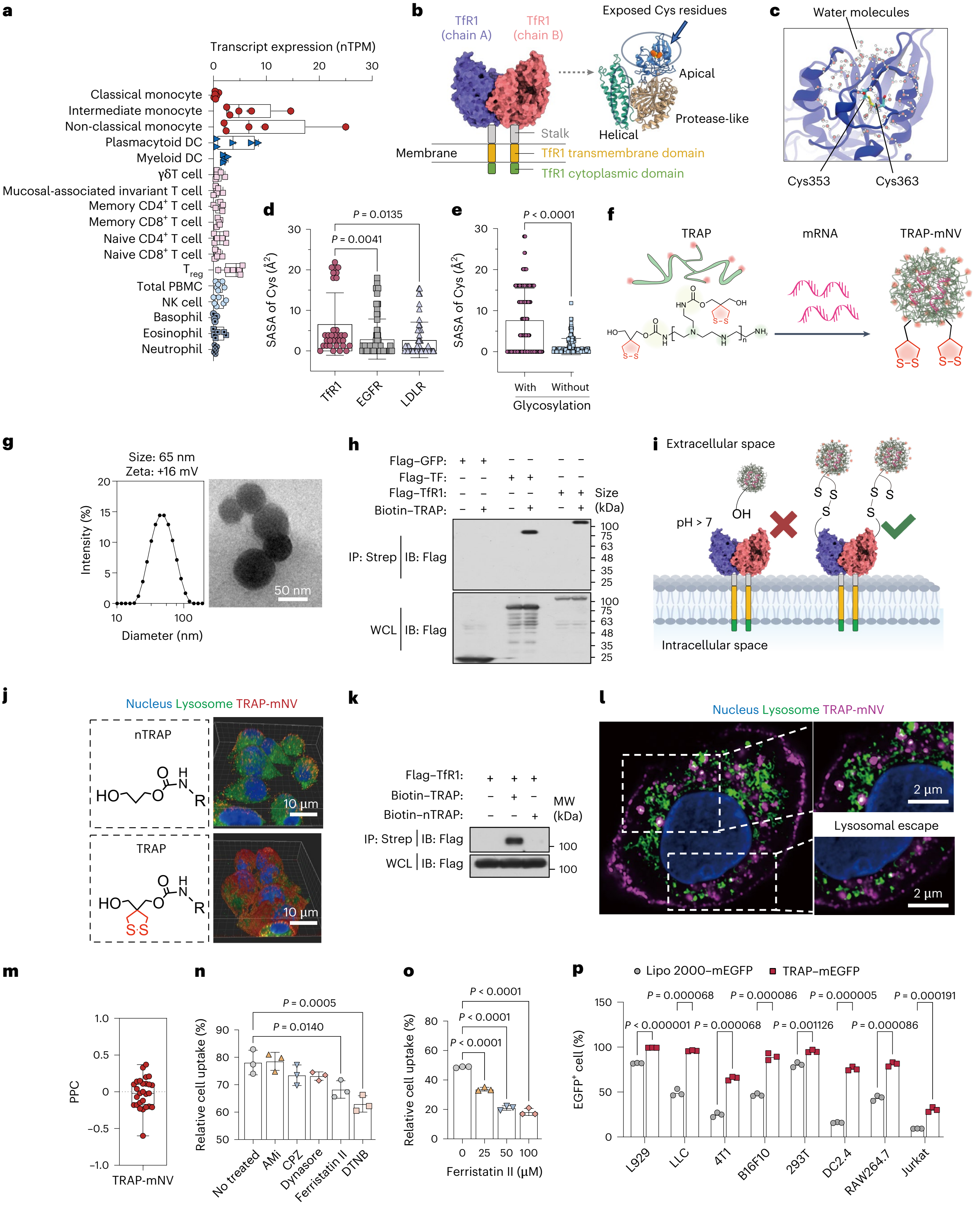
a
Transcript expression (nTPM)
0 10 20 30
Classical monocyte
Intermediate monocyte
Non-classical monocyte
Plasmacytoid DC
Myeloid DC
γδT cell
Mucosal-associated invariant T cell
Memory CD4+ T cell
Memory CD8+ T cell
Naive CD4+ T cell
Naive CD8+ T cell
Treg
Total PBMC
NK cell
Basophil
Eosinophil
Neutrophil
b
TfR1 (chain A)
TfR1 (chain B)
Exposed Cys residues
Apical
Protease-like
Helical
Stalk
Membrane
TfR1 transmembrane domain
TfR1 cytoplasmic domain
c
Water molecules
Cys353
Cys363
d
P = 0.0135
P = 0.0041
SASA of Cys (Å2)
0 10 20 30
TfR1
EGFR
LDLR
e
P < 0.0001
SASA of Cys (Å2)
0 10 20 30
With
Without
Glycosylation
f
TRAP
mRNA
TRAP-mNV
HO
O
HN
OH
S-S
N
H
n
NH2
g
Size: 65 nm
Zeta: +16 mV
Intensity (%)
0 5 10 15 20
10 100
Diameter (nm)
50 nm
h
Flag–GFP: + + – – – –
Flag–TF: – – + + – –
Flag–TfR1: – – – – + +
Biotin–TRAP: – + – + – +
Size (kDa)
IP: Strep | IB: Flag
WCL | IB: Flag
100 75 63 48 35 25
100 75 63 48 35 25
i
Extracellular space
pH > 7
OH
S S
S
S S
S
Intracellular space
j
Nucleus Lysosome TRAP-mNV
nTRAP
HO
O
O
H
N
R
10 μm
TRAP
HO
O
O
H
N
R
S·S
10 μm
k
Flag–TfR1: + + +
Biotin–TRAP: – + –
Biotin–nTRAP: – – +
MW (kDa)
IP: Strep | IB: Flag
WCL | IB: Flag
100
100
l
Nucleus Lysosome TRAP-mNV
2 μm
Lysosomal escape
2 μm
m
PPC
1.0 0.5 0 −0.5 −1.0
TRAP-mNV
n
P = 0.0005
P = 0.0140
Relative cell uptake (%)
50 60 70 80 90
No treated
AMi
CPZ
Dynasore
Ferristatin II
DTNB
o
P < 0.0001
P < 0.0001
P < 0.0001
Relative cell uptake (%)
0 20 40 60 80
0 25 50 100
Ferristatin II (μM)
p
Lipo 2000–mEGFP
TRAP–mEGFP
P = 0.000068
P = 0.000086
P = 0.000005
P = 0.000191
P < 0.000001
P = 0.000068
P = 0.001126
P = 0.000086
EGFP+ cell (%)
0 50 100 150
L929
LLC
4T1
B16F10
293T
DC2.4
RAW264.7
Jurkat

be synthesized by simply adjusting the feed ratio of DTC to PEI. The number of DTC grafts per unit of PEI polymer was further characterized by the specific ultraviolet absorption of the disulfide bonds at 330 nm (Supplementary Table. 1), and the ring-opening reaction of DTC was investigated by ^{1}H NMR spectroscopy (Supplementary Fig. 3b). The molar mass and degree of polymerization were determined by gel permeation chromatography (Supplementary Fig. 4).

TRAP is a biodegradable polycarbonate with dangling DTC groups that enhance nucleic-acid complexation and promote self-crosslinking during nanoparticle preparation, improving stability. To further assess the mRNA encapsulation efficiency and responsive release behaviour of TRAP, we conducted quantitative assays and electrophoretic analysis. TRAP exhibited a high mRNA encapsulation efficiency (>90%; Extended Data Fig. 1a). We next evaluated redox-triggered mRNA release by gel electrophoresis. After incubation in a reducing environment containing 10 mM glutathione (GSH), and competitive polyanions such as sodium heparin for 3 h, free mRNA was clearly released from TRAP (Extended Data Fig. 1b). In addition, kinetic analyses revealed a time- and condition-dependent release profile, with increasing release observed in reductive conditions (Extended Data Fig. 1c). To evaluate the impact of buffer and pH on TRAP assembly, we analysed particle size and zeta potential at different nucleic acid:polymer ratios (1:1, 3:1, 6:1 and 9:1). The 6:1 ratio produced the most reproducible results with the narrowest particle size distribution, suggesting it as the optimal formulation for TRAP–mRNA nanoparticles (Supplementary Fig. 5). The optimal buffer, *N*-2-hydroxyethylpiperazine-*N*′-2-ethanesulfonic acid (HEPE5.2), yielded TRAP–mRNA nanoparticles with a diameter of 60–70 nm and a zeta potential of +18 mV. TRAP–mRNA nanoparticles were confirmed to have a spherical shape through transmission electron microscopy (Fig. 1g). Gel electrophoresis demonstrated negligible nucleic-acid leakage (Supplementary Fig. 6a), and the particle size remained stable at room temperature for a week (Supplementary Fig. 6b,c), confirming efficient encapsulation and protective functionality in nucleic-acid delivery.

TRAP enhances mRNA internalization and transfection efficiency

Our study demonstrates that TRAP enhances cellular uptake and promotes the endosomal release of mRNA, thereby improving translation efficiency. Previous studies have shown that different uptake mechanisms can vary in efficiency, with membrane protein-mediated mRNA delivery emerging as a promising alternative to energy-intensive endocytosis[46–49]. Notably, thiol-mediated uptake was identified as a key mechanism[50], facilitated by enhanced binding to cell surface receptors. Confocal laser scanning microscopy (CLSM) revealed strong co-localization of TRAP with membrane-associated TfR1 (Supplementary Fig. 7), which suggests that nanoparticle uptake is partially dependent on TfR1. To further verify the binding ability of DTC-modified TRAP with TfR1, immunoprecipitation experiments were performed using green fluorescent protein (GFP) and transferrin proteins as controls. Both transferrin and TfR1 exhibited stronger binding than GFP (Fig. 1h). The SASA of transferrin was comparable to that of TfR1, whereas GFP had a SASA of almost zero (Supplementary Fig. 8), which explains the plausibility of binding to TRAP. These findings provide further support for the feasibility of achieving TRAP-specific binding by exploiting the differential expression of TfR1 across various cell types. Real-time CLSM imaging revealed a progressive increase in the fluorescence signal of cyanine5 (Cy5)-labelled mRNA on the cell membrane, indicating rapid nanoparticle adsorption (Supplementary Figs. 9a,b and 10). In conclusion, we demonstrated that DTC-modified TRAP enhances nanoparticle internalization by binding to cell-surface TfR1, promoting higher uptake (Fig. 1i).

In DC2.4 cells treated with TRAP (Cy5-labelled mRNA), distinct subcellular distributions were observed after lysosomal and nuclear staining. Cells treated with non-DTC-modified PEI-TMC (nTRAP)–mRNA exhibited numerous yellow co-localized spots (Supplementary Fig. 11), suggesting substantial lysosomal encapsulation of mRNA (red) within lysosomes (green). In contrast, TRAP-treated cells displayed a diffuse green signal throughout the cytoplasm, which is indicative of efficient lysosomal escape. Three-dimensional reconstructions allowed visualization of lysosomal co-localization in cells treated with nTRAP–mRNA and TRAP–mRNA (Fig. 1j); in addition, we validated the potential binding of nTRAP or TRAP to TfR1 through immunoprecipitation (Fig. 1k). Successful protein expression relies on the intracellular dissociation of mRNA from the polymer and its escape from the endosome. We dual-labelled the polymer and mRNA with distinct fluorophores to track this process. Substantial dissociation was observed as early as 2 h post incubation (Supplementary Fig. 12). Furthermore, we observed minimal co-localization of TRAP with lysosomes, indicating effective lysosomal escape (Fig. 1l and Supplementary Fig. 13). Quantitative Pearson's coefficient analysis confirmed efficient cytosolic release (Fig. 1m), a probable explanation for the enhanced mRNA transfection efficiency. In addition, we observed that TRAP-pretreated cells exhibited higher uptake of calcineurin, with a diffuse distribution of calcineurin observed at various time points (Supplementary Fig. 14). Previous studies suggest that the introduction of thiol groups induces transient membrane pore formation, which may contribute to the increased uptake of calcineurin[51–54]. Moreover, it has been shown that thiol groups facilitate endosomal escape of nanoparticles[55–57], indicating multiple potential mechanisms of TRAP's cellular internalization and its potential role in enhancing cell transfection.

To further elucidate the endocytosis mechanism, DC2.4 cells were pretreated with various inhibitors. After 1 h, inhibition of dynamin- and clathrin-mediated pathways substantially reduced nanoparticle uptake. Similarly, pretreatment with the sulfhydryl inhibitor 5,5′-dithiobis-(2-nitrobenzoic acid) (DTNB) or the TfR1 degradation agent ferristatin II suppressed nanoparticle internalization (Fig. 1n), indicating that sulfhydryl-associated membrane proteins mediate nanoparticle uptake. To explore the role of TfR1 in this process, DC2.4 cells were treated with ferristatin II at concentrations ranging from 0.1 μM to 100 μM for 4 h to induce TfR1 degradation. Western blot analysis confirmed a concentration-dependent reduction in TfR1 levels (Supplementary Fig. 15), and the nanoparticle internalization efficiency was closely correlated with TfR1 expression (Fig. 1o). No appreciable cytotoxicity at any of the tested concentrations was noted in cell viability assays (Supplementary Fig. 16).

We next evaluated the mRNA delivery efficiency of TRAP across different tumour and non-tumour cell lines. Compared with conventional transfection reagents, including Lipofectamine 2000 and Lipofectamine MessengerMAX, substantially enhanced EGFP expression was observed in most of the tested cell lines when TRAP was used as the delivery agent, as analysed by fluorescence microscopy and flow cytometry (Extended Data Fig. 1d–f, Fig. 1p and Supplementary Fig. 17), and TRAP resulted in negligible cytotoxicity (Supplementary Fig. 18). Notably, TRAP achieved over 80% transfection efficiency in RAW264.7 cells and substantially enhanced EGFP expression in other hard-to-transfect immune-cell types, including DCs (DC2.4) and Jurkat T cells, compared with Lipofectamine MessengerMAX. This superior performance is likely to be associated with the elevated expression of TfR1 (ref. 27), which facilitates efficient cellular uptake and endosomal escape in these cells.

Lymph node-selective mRNA delivery by TRAP

Lymph nodes are essential organs for lymphocyte residence, activation and proliferation, and are therefore critical for generating effective anticancer immune responses. Restricting mRNA expression to the injection site and its associated LNs can maximize immune activation while minimizing systemic toxicity[13,20,58–61]. To track the in vivo delivery efficiency of TRAP-based mRNA nanovaccines (TRAP-mNV), we encapsulated Cy5-labelled firefly luciferase (*Luc*) mRNA in TRAP and injected it subcutaneously into the base of the

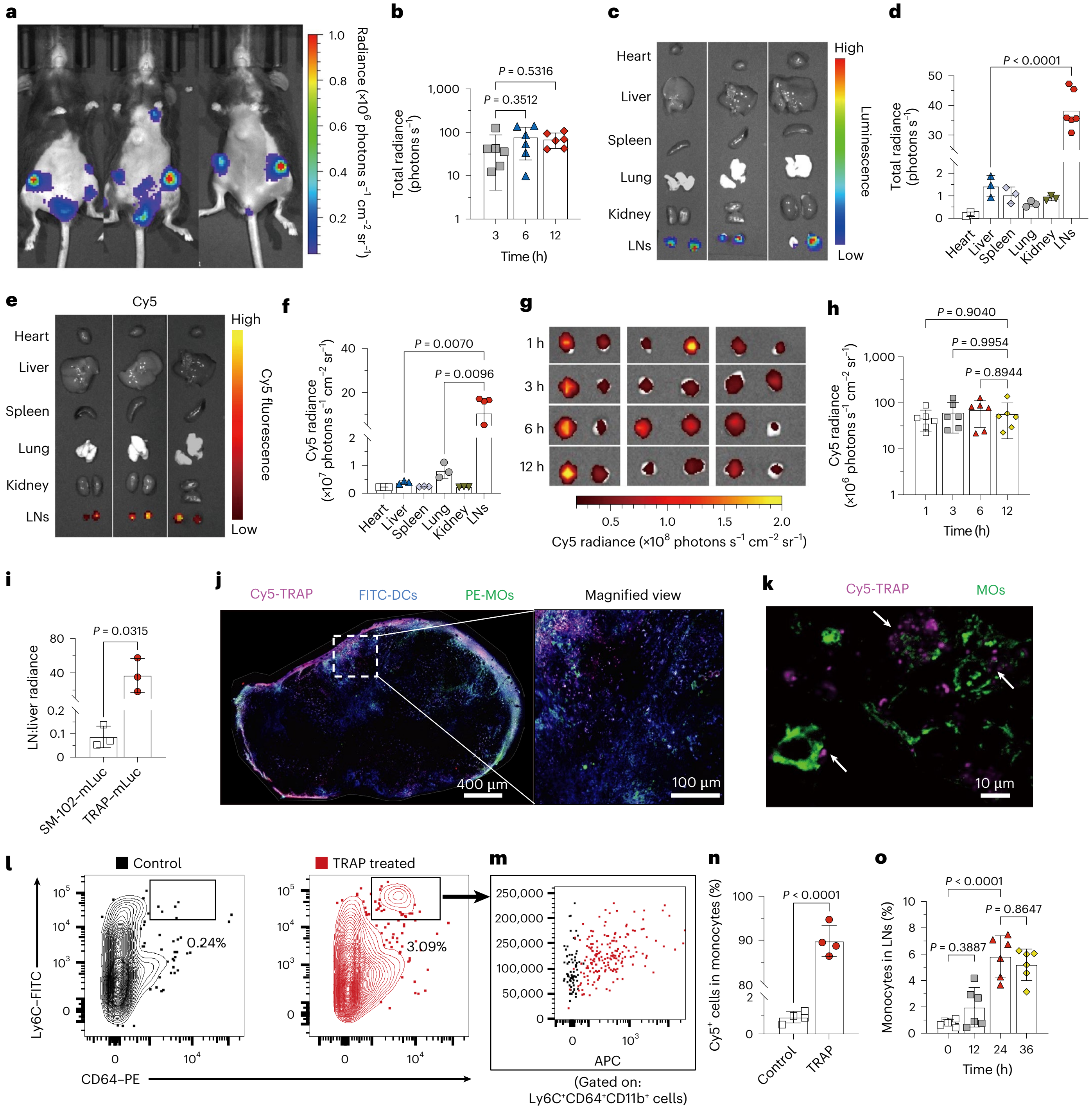

Fig. 2 | Monocyte-driven, lymph node-specific mRNA delivery and transfection. **a**, Representative bioluminescence images showing *Luc* mRNA expression in mouse LNs 6 h after subcutaneous administration of *Luc* mRNA-loaded TRAP (0.5 mg *Luc* mRNA kg^{-1}). **b**, Luminescence intensity in mouse LNs 3, 6 and 12 h post administration ($n = 6$ LNs from three mice). **c**, Representative ex vivo bioluminescence images of major organs collected from mice 6 h after subcutaneous administration. **d**, Luminescence intensity in the major organs in **c**. **e**, Representative fluorescence images of major organs collected 12 h after subcutaneous administration of Cy5-labelled TRAP–mLuc. **f**, Fluorescence intensity analysis of the major organs in **e**. **g**, Representative fluorescence images of LNs dissected from mice 1, 3, 6 and 12 h after subcutaneous administration of Cy5-labelled TRAP–mLuc. **h**, Fluorescence intensity analysis of the LNs in **g**. **g**,**h**, $n = 6$ LNs from three mice per time point. **i**, Luminescence intensity ratios in the live LNs relative to the liver 6 h following subcutaneous injection of TRAP–mLuc or SM-102–mLuc. **a**,**c**–**f**,**i**, $n = 3$ mice. **j**, Representative immunofluorescence images showing co-localization of Cy5-labelled TRAP-mNV with DCs and monocytes in LNs. **k**, Representative immunofluorescence images showing binding and internalization of Cy5-labelled TRAP-mNV by monocytes in LNs, the white arrows indicate adhesion and internalization of Cy5-labelled TRAP–mRNA complexes by monocytes. **j**,**k**, The experiments were independently repeated at least three times with similar results. **l**, Total monocytes in LNs were quantified by flow cytometry 6 h after subcutaneous injection. The percentage of cells in the gated regions in the flow cytometry plots are shown. **m**, Representative flow cytometry scatter plot showing uptake of Cy5-labelled TRAP by monocytes. Black dots, no uptake; red dots, uptake of Cy5-labelled TRAP–mRNA complexes. **n**, Percentage of monocytes positive for TRAP uptake ($n = 4$ biological samples). **o**, Proportion of monocytes in LNs 0, 12, 24 and 36 h after subcutaneous injection ($n = 6$ biological samples). **b**,**d**,**f**,**h**,**i**,**n**,**o**, Data are presented as the mean ± s.d. Statistical significance was determined using a one-way ANOVA (two-sided; **b**,**d**,**f**,**h**,**o**) or two-sided unpaired Student's *t*-test (**i**,**n**); exact *P* values are provided; NS, not significant. Source data are provided.

tail of C57BL/6 mice. Bioluminescence imaging was performed 3–12 h post injection to assess the biodistribution of TRAP and Luc expression levels. Notably, mRNA expression and nanoparticle localization were primarily confined to the injection site and the inguinal LNs (Fig. 2a). The fluorescence signals in the LNs remained stable up to 12 h following injection, indicating sustained LN-specific targeting and expression (Fig. 2b). Ex vivo organ imaging results further confirmed negligible accumulation and transfection in major organs such as the liver, heart, spleen, lungs and kidneys (Fig. 2c–f). Consistent with previous reports[13,14], TRAP exhibited an asymmetrical distribution across bilateral LNs. This phenomenon might be attributed to inter-individual variation in mice and remain elusive. Moreover, TRAP's LN-specific expression was highly reproducible across different mice, with consistent distribution levels over the 12-h period (Fig. 2g,h and Supplementary Fig. 19). In contrast, we found that mRNA expression of SM-102 LNPs mainly accumulated in the liver and at the injection site (Supplementary Fig. 20), and that TRAP greatly enhanced the specific delivery of mRNA, achieving an LN:liver ratio of 40 (Fig. 2i), in stark contrast to SM-102, which exhibited a ratio of <0.2. Therefore, we speculate that TRAP-mNV could enhance vaccination efficacy and reduce potential off-target toxicity of current LNP mRNA-based vaccine formulations. These findings underscore the potentials of TRAP for delivering mRNA-based cancer vaccines.

Antigen-presenting cells, including DCs, macrophages and monocytes, play pivotal roles in initiating immune responses following mRNA vaccine delivery. Dendritic cells capture and present the antigen to T cells in the LNs, whereas monocytes differentiate into antigen-presenting cells to support immune activation. This enhances antitumor immunity and generates long-lasting immune memory. We observed similar spatial distributions of DCs and monocytes in the LNs (Fig. 2j), with monocytes showing marked co-localization with Cy5-labelled TRAP-mNV. High-resolution imaging confirmed that monocytes efficiently internalized TRAP-mNV (Fig. 2k), indicating that they play a key role in driving nanoparticle lymphatic targeting. Moreover, we observed clear co-localization of TfR1 and TRAP-mNV in LNs (Supplementary Fig. 21), which suggests that monocytes efficiently capture nanoparticles via TfR1, thereby mediating LN targeting. Flow cytometric analysis of inguinal LNs following subcutaneous immunization revealed a substantial increase in monocyte proportions (Fig. 2l and Supplementary Fig. 22), with nearly 95% of monocytes internalizing TRAP-mNV and maintaining high levels from 24 to 36 h (Fig. 2m–o). To determine whether the increase in the proportion of monocytes in LNs is accompanied by enhanced TRAP–mRNA delivery and expression, we performed a series of quantitative analyses. Using tdTomato as a reporter in Ai9 mice, we noted that monocytes comprised the largest population (approximately 30%) of tdTomato$^+$ cells in the LNs, whereas DCs represented approximately 10% (Extended Data Fig. 2a–c). We then monitored the expression dynamics of mRNA-encoded surface Thy1.1 protein in Ly6C$^+$CD11c$^-$ monocytes at 3, 12 and 24 h post injection. A time-dependent increase in Thy1.1 expression was observed (Extended Data Fig. 2d–f), indicating accumulative mRNA translation in monocytes. Together, these findings provide quantitative and kinetic evidence that monocytes not only accumulate in LNs after TRAP–mRNA administration but also serve as a dominant cell population mediating mRNA translation in vivo. These findings support the hypothesis that monocytes drive TRAP-mNV lymphatic targeting, providing a promising strategy for mRNA vaccine delivery.

TRAP enhances monocyte recruitment following subcutaneous injection

To further investigate the underlying mechanisms of monocyte-driven trafficking, we analysed the immune response following subcutaneous injection (Fig. 3a). Subcutaneous administration of nTRAP did not lead to an obvious increase in local immune-cell populations, including Ly6C$^+$ monocytes, whereas TRAP induced marked recruitment of inflammatory monocytes (Extended Data Figs. 3a–c and 4a–c), resembling the inflammatory recruitment of monocytes and macrophages during microbial infection. Haematoxylin-and-eosin and immunohistochemistry staining confirmed the accumulation of CD11b$^+$ myeloid cells (Fig. 3b–d), with a slight decrease in abundance observed at 3 h (Fig. 3e), probably due to ongoing cell migration. Notably, a concurrent increase in CCR2 expression was detected, which is critical for regulating monocyte recruitment and migration to sites of inflammation[62,63]. This suggests that the transient reduction in CD11b$^+$ cells may be associated with CCR2-mediated mobilization, providing further support for its role in inflammatory cell trafficking. These findings indicate that DTC modification, rather than the PEI backbone alone, plays a critical role in initiating local innate immune responses and monocyte enrichment.

We next examined monocyte differentiation at the subcutaneous injection site following TRAP administration. Flow cytometry revealed that monocytes were the major cell type to uptake TRAP nanoparticles (Extended Data Fig. 4d). Differentiation was also observed within 8 h following injection in certain monocyte populations previous to their migration to LNs (Extended Data Fig. 4e). This phenotypic shift suggests that the differentiation of monocytes probably occurred at the injection site as well as the LN microenvironment.

To clarify the role of different phagocytes in TRAP trafficking, we used clodronate liposomes (CL-lipo) to deplete macrophages. No statistically significant reduction in Cy5 signal intensity was observed in LNs after CL-lipo treatment, indicating minimal involvement of macrophages in nanoparticle delivery (Supplementary Fig. 23). We further evaluated whether CL-lipo treatment affected Ly6C$^+$ monocytes by analysing immune-cell subsets in the peritoneum, blood and LNs. Flow cytometry confirmed that F4/80$^+$ tissue-resident macrophages were effectively depleted, whereas Ly6C$^+$CD11b$^+$ monocytes remained

Fig. 3 | Activation of the STING pathway by TRAP induces monocyte recruitment at the injection site. a, Illustration of TRAP-induced monocyte recruitment following subcutaneous injection. **b**, Representative images of mouse skin tissue collected at 0 (left) and 1 h (right) after subcutaneous injection of TRAP–mLuc and stained with haematoxylin and eosin. **c**, Proportion, determined by flow cytometry, of CD45$^+$ cells in skin tissues collected from the injection sites 1 h after administration ($n = 3$ biological samples). **d**, Representative immunohistochemistry images of CD11b (top) and CCR2 (bottom) staining of skin sections collected at 0, 1 and 3 h post injection. **e**, CD11b (left) and CCR2 (right) staining intensity in the immunohistochemistry images in **d**, calculated using ImageJ ($n = 6$ biological samples). **f**, Levels of TRAP uptake by the indicated immune cells at the injection site following subcutaneous injection ($n = 5$ biological samples). **g**, Representative flow cytometric profiles showing surface expression of CD80 and CD86 on BMDCs following treatment with the indicated formulations, including TRAP–mOVA and CpG. **h**, Proportions of CD80$^+$CD86$^+$ subpopulations among CD11c$^+$ BMDCs after the indicated treatments. **i**, Representative flow cytometry plots illustrating SIINFEKL peptide presentation by BMDCs exposed to the indicated formulations. **g**,**i**, The percentages of cells in the gated regions are indicated. **j**, Proportion of SIINFEKL-presenting BMDCs in the different treatment groups. **k**, Illustration of TRAP-induced activation of the STING pathway. **l**, Cytosolic mtDNA levels, determined by quantitative PCR analysis, in BMDCs following treatment with TRAP–mRNA. **m**, Concentrations of 2′3′-cGAMP, measured by ELISA, in BMDCs following treatment with TRAP–mRNA. **h**,**j**,**l**,**m**, $n = 3$ biological samples per group. **n**, Representative immunoblot analysis of the STING signalling pathway in BMDCs treated with TRAP–mRNA. MW, molecular weight; p-IRF3, phosphorylated IRF3; p-TBK1, phosphorylated TBK1. **c**,**e**,**f**,**h**,**j**,**l**,**m**, Data are presented as the mean ± s.d. Statistical significance was determined using a one-way ANOVA (two-sided; **e**,**f**,**h**,**j**,**l**) or a two-sided unpaired Student's *t*-test (**c**,**m**); exact *P* values are provided. **b**,**d**,**n**, The experiments were independently repeated at least three times with similar results. Panel **k** created in BioRender: Ren, Q. https://biorender.com/w1ycrg6 (2026). Source data are provided.

unaffected across all tissues examined (Extended Data Fig. 5b–e), demonstrating that monocyte-mediated TRAP delivery was preserved.

Notably, flow cytometry analyses demonstrated that 80% of the Ly6C$^+$ inflammatory monocytes internalized Cy5-labelled mRNA, far exceeding uptake by other immune cells (Fig. 3f). This high uptake correlated with elevated TfR1 expression on monocytes, providing support for a TfR1-dependent internalization mechanism. Collectively, these findings suggest that TRAP enhances monocyte recruitment and uptake at the injection site, thereby promoting their migration to draining LNs and enabling efficient, targeted immune activation. Adjuvant-like mRNA delivery vectors can amplify the strength and duration of immune responses, providing more effective antitumour or anti-infection immunity, given that adjuvants might stimulate monocyte migration to LNs[64]. We first investigated the ability of TRAP to stimulate DC maturation by co-incubating TRAP–ovalbumin mRNA (TRAP–mOVA) with bone marrow-derived DCs (BMDCs).

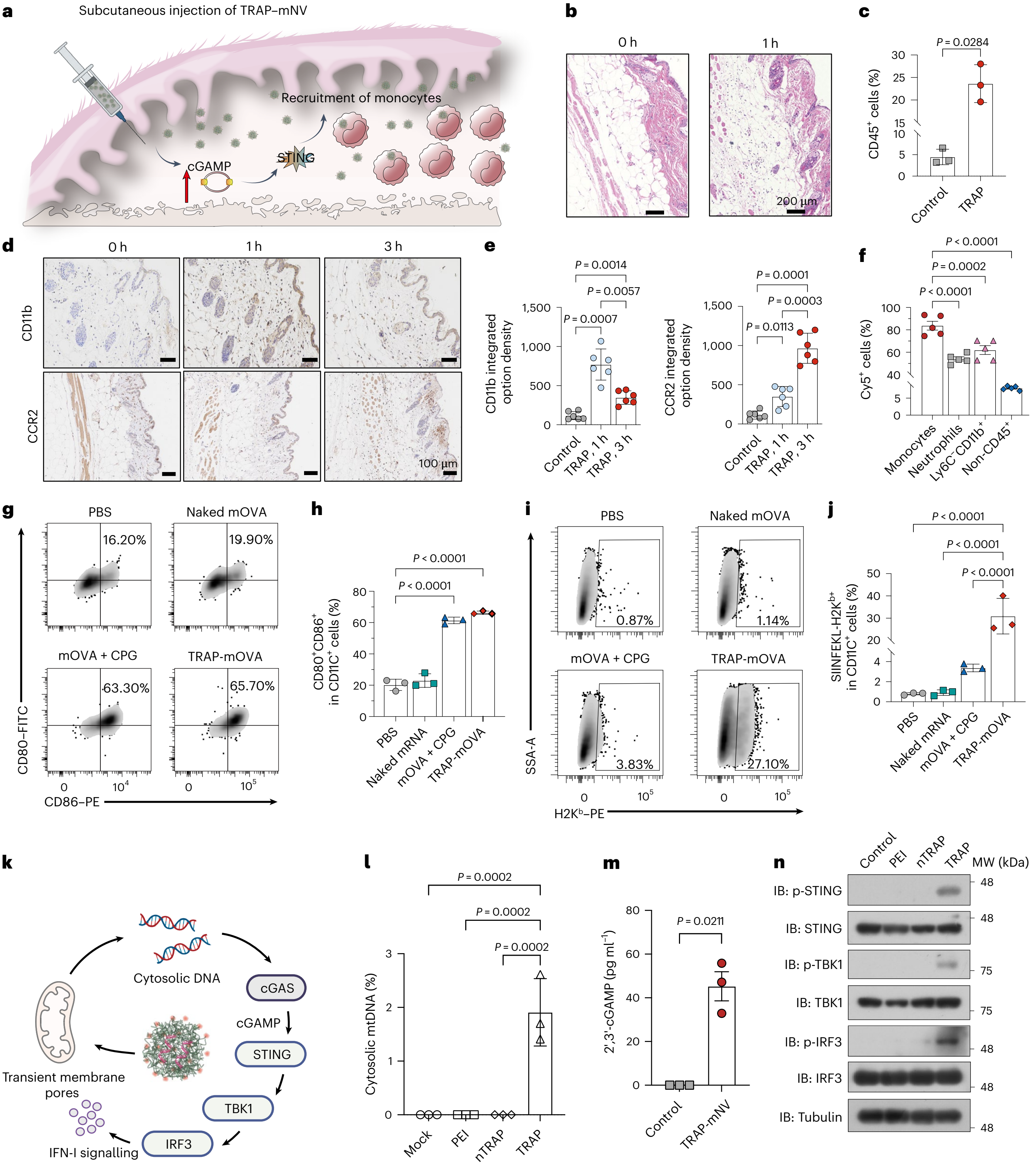

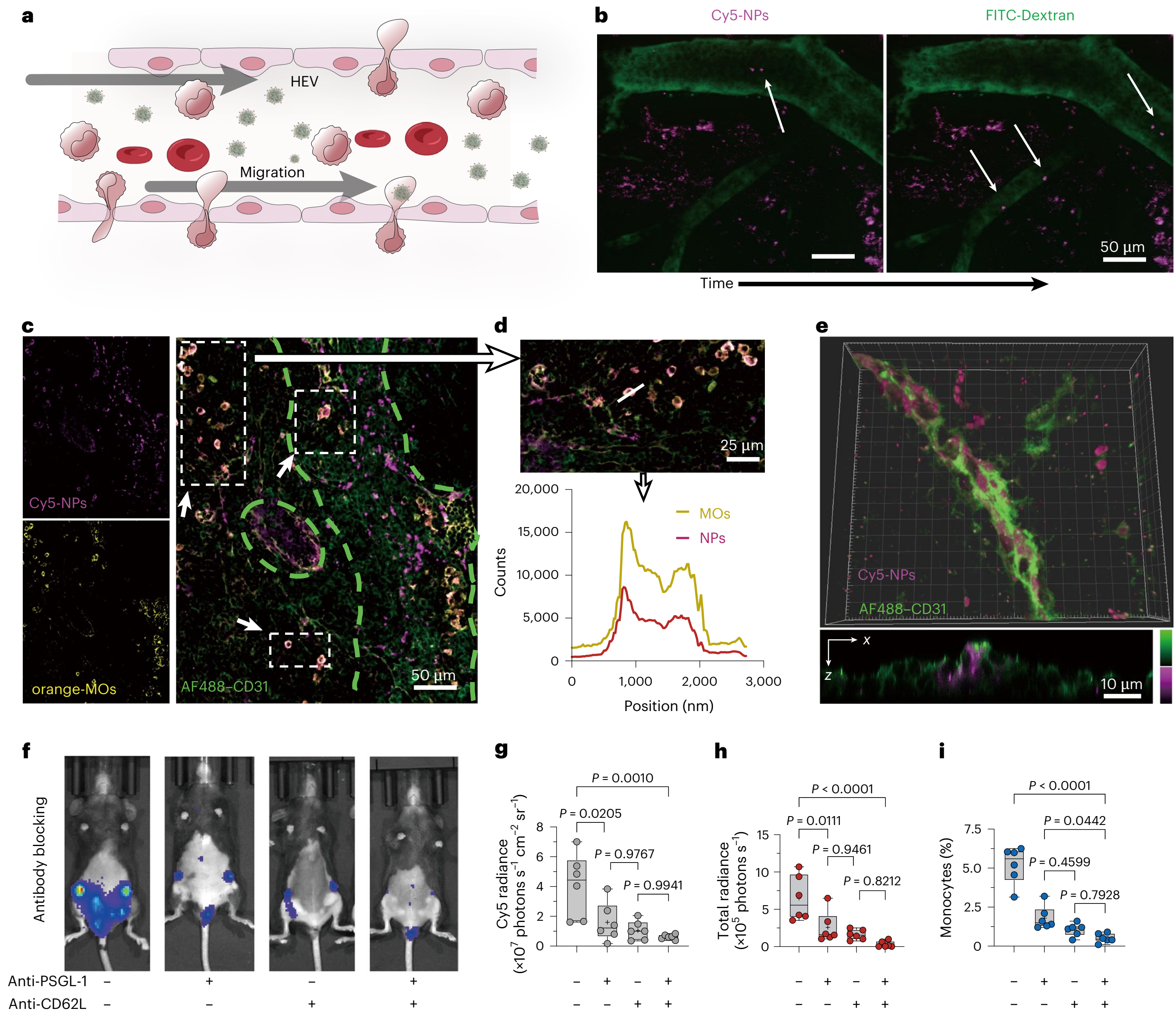

Fig. 4 | High endothelial venule-mediated recruitment of TRAP-mNV into the lymph nodes. a, Illustration of TRAP-mNV migration into LNs. **b**, Mice were subcutaneously injected with TRAP–mRNA and intravenously injected with fluorescein isothiocyanate (FITC)-labelled dextran, followed by intravital microscopy imaging 30 min post administration. Representative time-lapse images show the intravascular migration of TRAP–mRNA, the white arrows indicate migration of TRAP–mRNA in blood vessels. **c**, Representative immunofluorescence images of LNs collected 12 h after subcutaneous injection of Cy5-labelled TRAP–mRNA, the white arrows indicate regions showing co-localization of TRAP nanoparticles with monocytes in the lymph node, and dashed green lines outline vasculature. **d**, Magnified view of the top-left dashed box in **c** highlighting the strong spatial overlap between monocytes (MOs) and TRAP–mRNA nanoparticles (top). Lower panel shows the colocalization profile of line-crossing region indicated in the upper figure. **e**, Representative three-dimensional reconstructed images (Imaris) showing the spatial distribution of TRAP–mRNA and blood vessels in LNs. **b**–**e**, The experiments were independently repeated at least three times with similar results. **f**, Representative in vivo bioluminescence images showing *Luc* mRNA expression in mouse LNs subjected to antibody blocking with/without anti-PSGL and anti-CD62L ($n = 3$ mice per group). **g**, Intensity of Cy5 fluorescence in LNs. **h**, Intensity of Luc bioluminescence intensity in LNs. **i**, Percentage of monocytes in LNs, determined by flow cytometry. **g**–**i**, Data are presented as box-and-whisker plots, where the box represents the interquartile range (25th–75th percentiles), with the whiskers extending to the minimum and maximum values, the line in the box indicating the median, and all individual data points displayed. Statistical significance was determined using a one-way ANOVA (two-sided); $n = 3$ mice per group, six LNs per group. AF488, Alexa Fluor 488; NP, nanoparticle. Source data are provided.

TRAP significantly upregulated the expression of co-stimulatory molecules CD80 and CD86, similar to CPG, a well-known immunostimulant (Fig. 3g,h and Supplementary Fig. 24). Unlike CPG, which induces DC activation but lacks antigen delivery capability, TRAP–mOVA markedly boosted BMDC maturation and antigen presentation (Fig. 3i,j and Supplementary Fig. 25), highlighting its dual function as both a delivery vehicle and an immune stimulator. To understand the mechanism underlying TRAP's effect on DC maturation, CLSM co-localization analysis confirmed a strong spatial association between TRAP and mitochondria (Supplementary Fig. 26a). In addition, TRAP–mRNA treatment induced elevated cytosolic mitochondrial DNA (mtDNA) levels compared with the control groups (Fig. 3l,m and Supplementary Fig. 26b). In BMDCs and RAW264.7 cells, TRAP induced strong phosphorylation of TBK1 and IRF3 (Fig. 3n and Supplementary Fig. 26c).

High endothelial venule-mediated recruitment of TRAP-mNV into the lymph nodes

We observed that inflammation at the injection site promoted the recruitment of monocytes, which subsequently migrated to the LNs via HEVs (Fig. 4a and Supplementary Fig. 27a). The mechanisms underlying this monocyte trafficking are of particular interest. In vivo imaging of the LNs revealed the dynamic migration of TRAP-mNV within the vasculature (Fig. 4b). CD31 staining further confirmed that TRAP-mNV migrated via blood vessels (Fig. 4c). Meanwhile, co-localization of monocytes with TRAP was clearly visible in immunofluorescently stained samples (Fig. 4d and Supplementary Fig. 27b). Three-dimensional reconstruction provided clearer visualization of the uniform distribution of TRAP-mNV within the vessels (Fig. 4e). These findings demonstrate that following subcutaneous immunization, monocytes and other recruited cells internalize TRAP-mNV and migrate through the vasculature to the LNs, where they efficiently express the target protein. To examine whether TRAP nanoparticles selectively engage with monocytes for LN homing, we analysed myeloid cell subsets at the injection site at multiple time points post injection[65]. Flow cytometric profiling revealed that monocytes represented the dominant population among recruited myeloid cells from 3 h to 24 h, far exceeding the numbers of DCs and macrophages (Extended Data Fig. 6a). Moreover, monocytes also represented the major immune cells actively translating TRAP–mRNA, as examined in Thy1.1$^+$ cell populations across all time points (Extended Data Fig. 6b). These results collectively underscore the selective enrichment and functional engagement of monocytes in TRAP-mediated LN targeting.

To further confirm this, we injected a blocking antibody targeting P-selectin glycoprotein ligand-1 (PSGL-1), an adhesion molecule essential for trafficking to inflamed peripheral tissues. PSGL-1 blockade led to a reduction in *Luc* mRNA expression in the LNs and a decrease of >50% in monocyte recruitment (Fig. 4f,g), indicating that monocyte trafficking to the LNs primarily occurs via peripheral tissues. To assess the possibility of direct monocyte migration through HEVs, we administered the blocking antibody anti-CD62L during immunization, as CD62L is critical for HEV-mediated trafficking. Blockade of CD62L resulted in a substantial reduction in monocyte migration. Combined blockade of PSGL-1 and CD62L led to a further decrease, with almost complete loss of *Cy5* mRNA fluorescence in the LNs and no detectable Luc expression (Fig. 4h,i). These findings indicate that TRAP migration to LNs is closely linked to inflammatory monocytes, with HEV-mediated entry as the primary route for monocyte recruitment to the LNs following subcutaneous immunization.

TRAP-mNV drives monocyte-to-dendritic cell differentiation to promote immune responses

Previous studies showed that nanoparticles, especially those inducing inflammation, are preferentially taken up by monocytes, which then differentiate into macrophages or monocyte-derived DCs, thereby enhancing mRNA delivery[66,67]. Following TRAP-mNV immunization, flow cytometry analysis demonstrated that monocytes produced higher levels of IL-12 compared with DCs (Fig. 5a). To investigate whether further enhancing IL-12 expression in monocytes could potentiate the immune response and promote monocyte differentiation, we employed a co-delivery strategy of antigen and *IL-12* mRNA (mIL-12). The results indicated that co-delivery of IL-12 did not increase the proportion of monocytes in the LNs, possibly due to the mild early expression at the injection site, which failed to induce notable cytokine secretion (Fig. 5b). We monitored the expression of CD11c and MHC-I on Ly6C$^+$ monocytes over time in the LNs (Supplementary Figs. 28 and 29). A progressive increase in the expression of both markers was observed (Fig. 5c,d), indicating that these monocytes may differentiate into antigen-presenting cells. Notably, we identified a Ly6C$^+$CD11c$^+$XCR1$^{+/-}$ population at the injection site following TRAP administration (Extended Data Fig. 4e,f). Several studies have shown that Ly6C$^+$ monocytes can differentiate into monocyte-derived DCs in response to inflammatory cues, and these monocyte-derived DCs possess antigen-presenting capabilities[32,67]. Although XCR1 is a canonical marker of cDC1, it can also be upregulated on monocyte-derived DCs under inflammatory conditions, suggesting a phenotypic convergence towards cross-presenting cDC1-like states[68–70]. These findings collectively support the idea that monocytes, after TRAP uptake, may not only serve as initial mRNA carriers but can also functionally contribute to antigen presentation and immune activation, either directly or through differentiation into XCR1$^+$ monocyte-derived DCs.

Importantly, co-delivery of mIL-12 seemed to enhance this differentiation process, probably through IL-12-induced interferon (IFN)-γ secretion[71]. This creates a positive-feedback loop that amplifies cytokine production in the LNs, further enhancing antigen-presenting-cell function[71,72]. These findings suggest that co-delivery of IL-12 and antigen mRNA to LN represents a more feasible approach for enhanced immune responses. Moderately regulated cytokine secretion in the LNs is critical for initiating and sustaining cell-mediated immune responses[73–75]. However, excessive cytokine release can result in a cytokine storm, potentially leading to immune overactivation and systemic inflammation, posing safety risks[76,77]. To assess this, we measured IFN-γ secretion in the LNs and serum of mice 24 h post immunization using the LEGENDplex MU inflammatory panel (Fig. 5e,f). We also quantified other pro-inflammatory cytokines, such as TNF, IL-12p70 and IL-1β, along with additional cytokines, including IL-27, IL-10 and IL-1α (Supplementary Fig. 30). Notably, minimal systemic exposure to TRAP ensured that no cytokine storm occurred, confirming the safety of this vaccination strategy. Furthermore, co-delivery of IL-12 and mOVA resulted in the upregulation of several cytokines, including IFN-γ, which is crucial for enhancing antigen presentation. We also observed increased levels of MCP-1 and GM-CSF, both of which are key mediators of monocyte recruitment to the LNs. MCP-1 facilitates monocyte migration[78,79], and GM-CSF plays an essential role in their differentiation and activation[80],

Fig. 5 | TRAP-mNV drives monocyte-to-dendritic cell differentiation to promote immune responses. **a**, Percentage of IL-12$^+$ DCs and monocytes in the subcutaneous tissue (left) and LNs (right) of mice, as determined by flow cytometry. **b**,**c**, Percentage of monocytes in LNs (**b**; *n* = 6 biological samples) and surface expression of MHC-I on monocytes at 0, 12, 24 and 36 h after treatment with TRAP–mOVA or TRAP–mOVA + mIL-12 (**c**; *n* = 5 biological samples). MFI, mean fluorescence intensity. **d**, Percentage of CD11c$^+$ monocytes in LNs detected by flow cytometry (*n* = 5 biological samples). **e**,**f**, Concentrations of cytokines (IFN-γ, IL-12p70, GM-CSF, MCP-1 and IL-6) measured in the LNs (**e**) and serum (**f**) of vaccinated mice treated with TRAP–mOVA or TRAP–mOVA + mIL-12 (*n* = 3 biological samples). **g**, Experimental scheme of subcutaneous immunization with PBS, naked OVA, TRAP–mOVA, TRAP–mLuc, TRAP–mIL-12 or TRAP–mOVA + mIL-12, followed by flow cytometric analysis of LNs on day 3 and spleens on day 14 post immunization. **h**,**i**, Representative flow cytometry plots (**h**) and percentage (**i**) of CD80$^+$CD86$^+$ DCs in the LNs. **j**, Percentage of SIINFEKL-presenting DCs in the LNs. **k**,**l**, Percentage of IFN-γ$^+$ cells in CD3$^+$CD8$^+$ T (**k**) and CD3$^-$NK1.1$^+$ (**l**) subpopulations seven days after the second vaccination. **m**,**n**, Representative flow cytometry plots (**m**) and percentage (**n**) of CD3$^+$CD8$^+$Tetramer$^+$ T cells binding to H-2K^b OVA tetramer–SIINFEKL in the mouse spleen seven days after the second vaccination. **h**,**m**, The percentages of cells in the quadrants of interest are shown. **a**,**h**–**m**, *n* = 6 biological samples. **o**, ELISpot images (left; colour-coded as in **h**–**n**) and spot numbers (right) of IFN-γ-secreting T cells in the spleens of vaccinated mice (*n* = 4 biological samples). **a**–**f**,**i**–**l**,**n**,**o**, Data are presented as the mean ± s.d. Statistical significance was determined using a two-sided unpaired Student's *t*-test (**a**), two-way ANOVA (**b**,**c**) or one-way ANOVA (two-sided; **d**–**f**,**i**–**l**,**n**,**o**); exact *P* values are provided; NS, not significant. MOs, monocytes. Source data are provided.

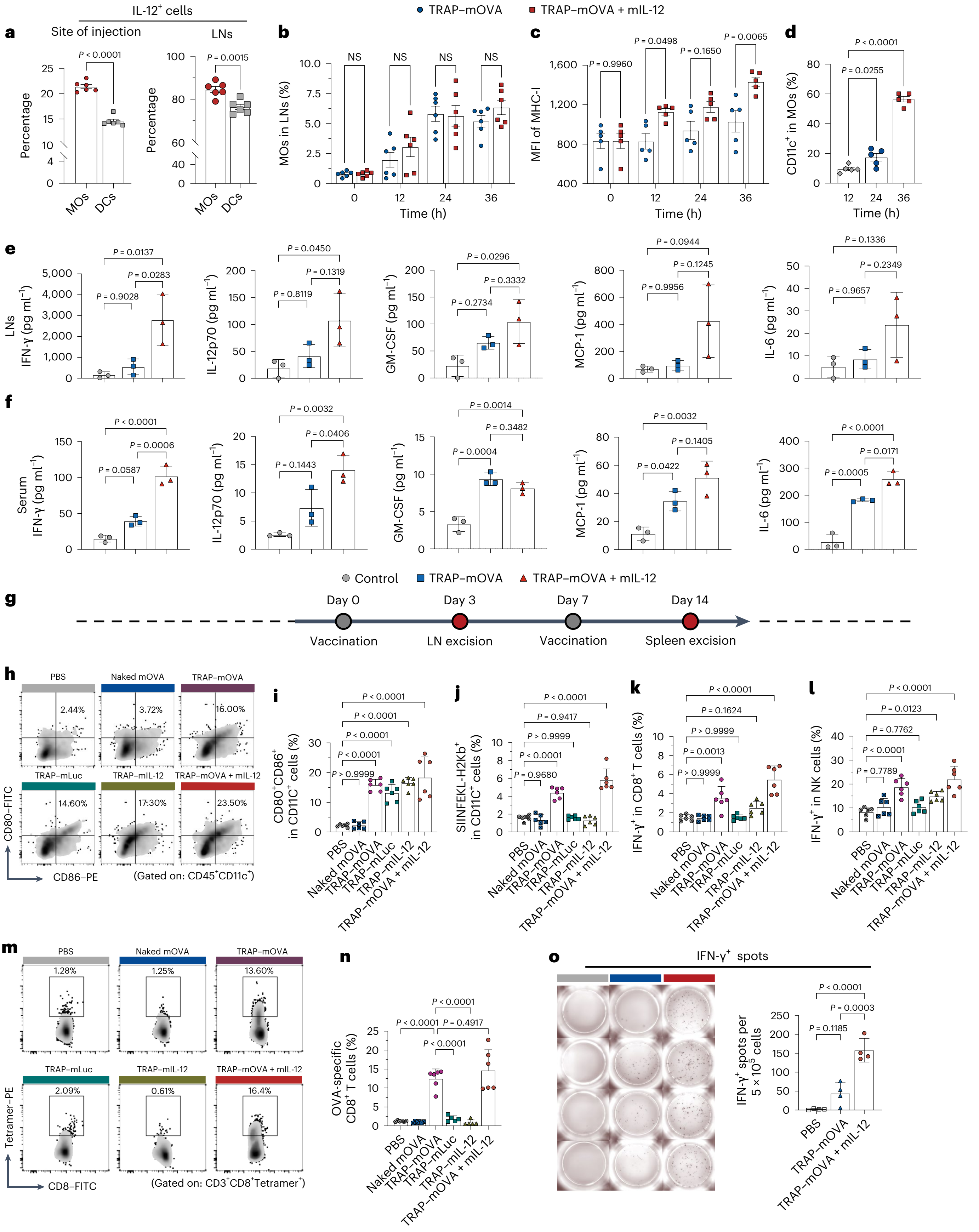
a
IL-12$^+$ cells
Site of injection
LNs
Percentage
MOs
DCs
P < 0.0001
P = 0.0015
b
● TRAP–mOVA
■ TRAP–mOVA + mIL-12
MOs in LNs (%)
NS
Time (h)
0
12
24
36
c
MFI of MHC-I
P = 0.9960
P = 0.0498
P = 0.1650
P = 0.0065
Time (h)
d
CD11c$^+$ in MOs (%)
P < 0.0001
P = 0.0255
Time (h)
e
LNs
IFN-γ (pg ml^{-1})
P = 0.0137
P = 0.0283
P = 0.9028
IL-12p70 (pg ml^{-1})
P = 0.0450
P = 0.1319
P = 0.8119
GM-CSF (pg ml^{-1})
P = 0.0296
P = 0.3332
P = 0.2734
MCP-1 (pg ml^{-1})
P = 0.0944
P = 0.1245
P = 0.9956
IL-6 (pg ml^{-1})
P = 0.1336
P = 0.2349
P = 0.9657
f
Serum
IFN-γ (pg ml^{-1})
P < 0.0001
P = 0.0006
P = 0.0587
IL-12p70 (pg ml^{-1})
P = 0.0032
P = 0.0406
P = 0.1443
GM-CSF (pg ml^{-1})
P = 0.0014
P = 0.3482
P = 0.0004
MCP-1 (pg ml^{-1})
P = 0.0032
P = 0.1405
P = 0.0422
IL-6 (pg ml^{-1})
P < 0.0001
P = 0.0171
P = 0.0005
● Control
■ TRAP–mOVA
▲ TRAP–mOVA + mIL-12
g
Day 0
Day 3
Day 7
Day 14
Vaccination
LN excision
Vaccination
Spleen excision
h
PBS
Naked mOVA
TRAP–mOVA
2.44%
3.72%
16.00%
TRAP–mLuc
TRAP–mIL-12
TRAP–mOVA + mIL-12
14.60%
17.30%
23.50%
CD80–FITC
CD86–PE
(Gated on: CD45$^+$CD11c$^+$)
i
CD80$^+$CD86$^+$ in CD11C$^+$ cells (%)
P < 0.0001
P < 0.0001
P < 0.0001
P < 0.0001
P > 0.9999
j
SIINFEKL-H2Kb$^+$ in CD11C$^+$ cells (%)
P < 0.0001
P = 0.9417
P > 0.9999
P < 0.0001
P = 0.9680
k
IFN-γ$^+$ in CD8$^+$ T cells (%)
P < 0.0001
P = 0.1624
P > 0.9999
P = 0.0013
P > 0.9999
l
IFN-γ$^+$ in NK cells (%)
P < 0.0001
P = 0.0123
P = 0.7762
P < 0.0001
P = 0.7789
PBS
Naked mOVA
TRAP–mOVA
TRAP–mLuc
TRAP–mIL-12
TRAP–mOVA + mIL-12
m
PBS
Naked mOVA
TRAP–mOVA
1.28%
1.25%
13.60%
TRAP–mLuc
TRAP–mIL-12
TRAP–mOVA + mIL-12
2.09%
0.61%
16.4%
Tetramer–PE
CD8–FITC
(Gated on: CD3$^+$CD8$^+$Tetramer$^+$)
n
OVA-specific CD8$^+$ T cells (%)
P < 0.0001
P < 0.0001
P = 0.4917
P < 0.0001
o
IFN-γ$^+$ spots
IFN-γ$^+$ spots per 5 × 10^5 cells
P < 0.0001
P = 0.0003
P = 0.1185
PBS
TRAP–mOVA
TRAP–mOVA + mIL-12

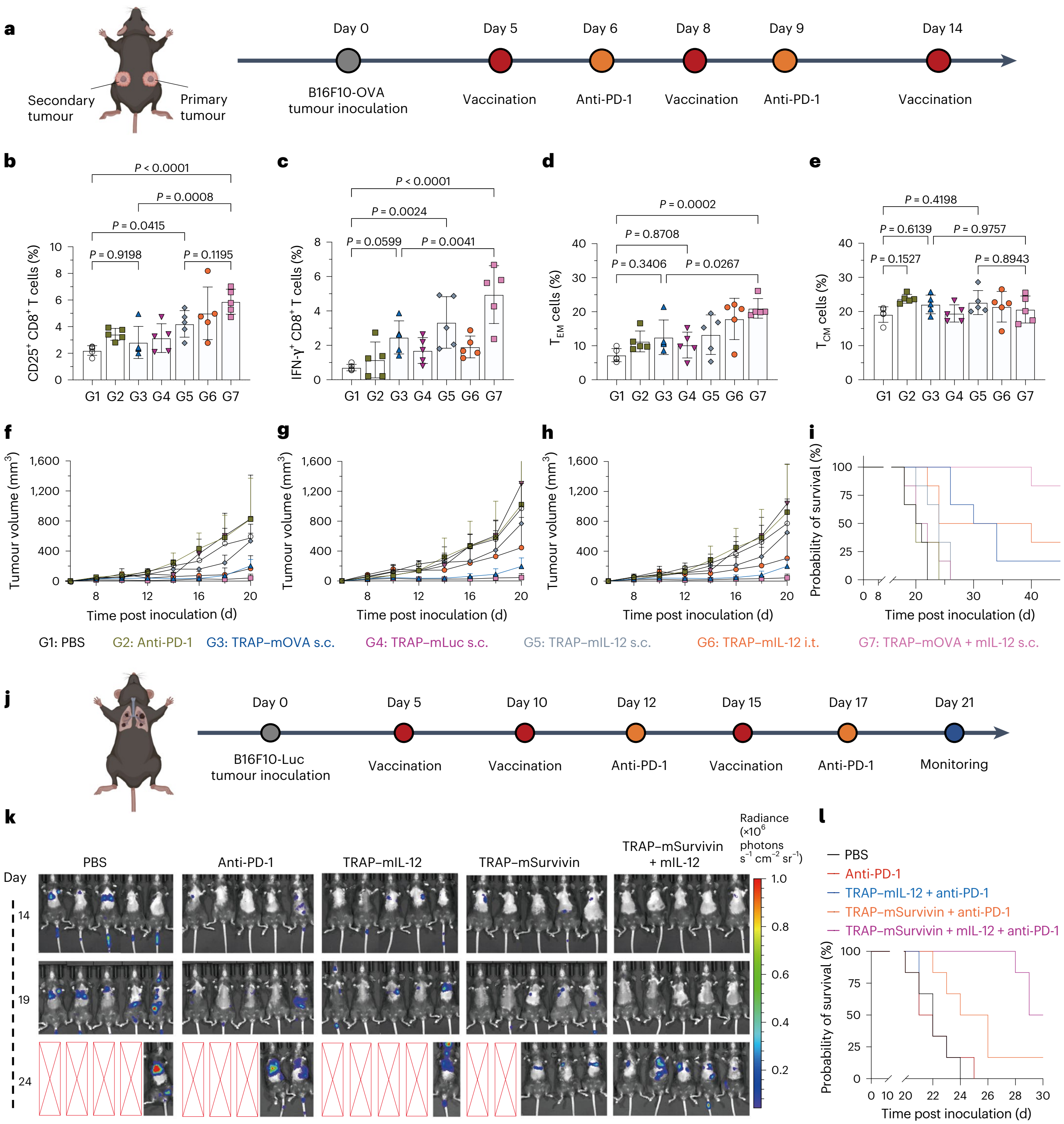

Fig. 6 | Therapeutic effect of TRAP-mNV vaccination on the B16F10 tumour model. a, Experimental time line for tumour inoculation and vaccination. **b**,**c**, Percentage of CD25$^+$ (**b**) and IFN-γ$^+$ (**c**) CD8$^+$ T cells 14 days after the first vaccination with the indicated formulations ($n = 5$ mice per group). **d**,**e**, Percentage of memory T cells in the peripheral blood of the mice analysed by flow cytometry based on CD44 and CD62L surface expression (**d**, T_{EM}, CD44$^+$CD62L$^-$; **e**, T_{CM}, CD44$^+$CD62L$^+$; $n = 5$ mice per group). **f**,**g**, Tumour growth curves of B16F10-OVA tumour-bearing mice treated with the indicated formulations, with primary intratumoral injection of TRAP–mIL-12 (**f**) or without intratumoral TRAP–mIL-12 injection (**g**; $n = 6$ mice per group). **h**,**i**, Summary of tumour growth curves (primary + secondary; **i**) and survival curves of B16F10-OVA tumour-bearing mice treated with the indicated formulations ($n = 6$ mice per group). **b**–**i**, Definitions of the colour-coded formulations G1–7 are provided beneath the panels; i.t., intratumoral delivery; s.c. subcutaneous delivery. **j**, Experimental time line of nanovaccine treatment with TRAP loaded with Survivin mRNA (TRAP–mSurvivin) combined with anti-PD-1 therapy. **k**, In vivo bioluminescence images of B16F10-Luc tumour-bearing mice treated with the indicated formulations; red boxes indicate mice that succumbed to tumour burden ($n = 5$ mice per group). **l**, Survival curves of B16F10-Luc tumour-bearing mice during the 30-day observation period ($n = 6$ mice per group). Dose: 2 μg mIL-12 + 10 μg mOVA per injection. **b**–**h**, Data are presented as the mean ± s.d. **b**–**h**,**i**,**l**, Statistical significance was determined using an ordinary one-way ANOVA (two-sided; **b**–**e**) or the log-rank Mantel–Cox test (**i**,**l**); exact P values are provided. Illustrations in **a** and **j** created in BioRender: Ren, Q. https://BioRender.com/5ctdmo3 (2026). Source data are provided.

providing further support for the monocyte-mediated targeted delivery of TRAP to the LNs.

Three days following subcutaneous immunization, we analysed T cell responses to investigate adaptive immune activation (Fig. 5g). Flow cytometry revealed that TRAP-mNV increased the proportion of mature DCs in the LNs (Fig. 5h,i and Supplementary Fig. 31). As a control, TRAP-mNV loaded with firefly *Luc* mRNA (TRAP–mLuc) also promoted DC maturation but did not induce OVA antigen presentation, similar to PBS treatment. In contrast, co-delivery of IL-12 and mOVA further enhanced both DC maturation and OVA antigen presentation (Fig. 5j and Supplementary Fig. 32). This effect was probably driven by IL-12-induced IFN-γ secretion by T cells and other LN-resident immune cells, consistent with earlier findings[71]. Moreover, co-delivery increased intracellular IFN-γ production in CD8$^+$ T and natural killer (NK) cells (Fig. 5k,l and Supplementary Figs. 33 and 34). Co-delivery also remarkably boosted the frequency of OVA-specific CD8$^+$ T cells in the spleen (Fig. 5m,n and Supplementary Fig. 35). ELISpot assays confirmed the presence of IFN-γ-secreting T cells in the spleen, in agreement with the increased frequency of SIINFEKL-specific CD8$^+$ T cells. Unimmunized mice showed no response to SIINFEKL, whereas all vaccinated groups generated IFN-γ-secreting T cells to varying degrees, with the highest levels observed in the co-delivery group (Fig. 5o), suggesting that this mRNA vaccine formulation induces a more robust T cell-mediated immune response.

TRAP-mNV induces a potent and durable effect against cancer

To further assess the potency of the TRAP cancer vaccine in stimulating systemic antitumour immune response, we compared the efficacy of the cancer treatment by administering cancer vaccine intratumorally and subcutaneously. As detailed in Fig. 6a, we subcutaneously inoculated B16F10-OVA cells into both the left and right flanks of mice on day 0, followed by vaccination on days 5, 8 and 14. In addition, one group was administered anti-PD-1 therapy on days 6 and 9. Intriguingly, the group receiving LN-targeted transfection of mOVA and mIL-12 exhibited a markedly higher percentage of IFN-γ$^+$CD8$^+$ T cells, with the co-administration of mOVA and mIL-12 further enhancing CD25$^+$CD8$^+$ and IFN-γ$^+$CD8$^+$ T cell production (Fig. 6b,c and Supplementary Figs. 36,37). *IL-12* mRNA alone also led to an increased proportion of IFN-γ$^+$CD8$^+$ T cells but these T cells were not antigen-specific. We assessed the immune memory effect by analysing CD8$^+$ T cells in whole blood after immunization to determine the proportion of memory T cells (Supplementary Fig. 38). The combination treatment markedly increased the percentage of effector memory T (T_{EM}) cells compared with the saline group and monotherapy groups (Fig. 6d). The negligible difference in the number of central memory T (T_{CM}) cells may be due to the fact that T_{CM} cells are mainly produced in lymphoid organs such as the spleen (Fig. 6e).

We speculated that LN-targeted delivery of cancer vaccine and IL-12 would elicit a more robust systemic antigen-specific immune response. Although intertumoral delivery effectively inhibited tumour growth at the injection site, its impact on distal tumours was limited (Fig. 6f–h). In contrast, subcutaneous delivery of mIL-12 alone had no obvious effect on tumour growth at either flank. However, when combined with mOVA for synergistic LN delivery, robust tumour growth suppression was observed bilaterally, emphasising the critical role of OVA-specific T cells. These findings underscore the importance of the co-administration of mIL-12 for enhancing the therapeutic efficacy of the mRNA vaccine. Three mice in the group with combined anti-PD-1 treatment exhibiting the strongest T cell responses achieved complete remission (Fig. 6i), indicating that combining mRNA vaccines with check-point inhibitors provides substantial therapeutic benefits. Antitumour efficacy was further evaluated in metastatic B16F10 models using Survivin as a tumour-associating antigen (Fig. 6k,l). Immunization with the TRAP–mRNA vaccine in combination with mIL-12 notably prolonged survival in both models, further highlighting its broad therapeutic potential.

To further assess the generalizability of TRAP-mNV, we employed the human papillomavirus (HPV)-driven TC-1 tumour model. Mice were subcutaneously immunized with TRAP–*HPV* mRNA (mHPV) formulations on days 0, 3 and 10 (Fig. 7a). TRAP vaccination markedly delayed tumour growth and extended overall survival (Fig. 7b). Beyond its therapeutic efficacy, TRAP vaccination increased the frequency of CD69$^+$ activated CD8$^+$ T cells in the spleen and LNs (Fig. 7c,d), enhanced the abundance of HPV E7 tetramer$^+$CD8$^+$ T cells in the spleen (Fig. 7e) and promoted IFN-γ$^+$CD8$^+$ T cell responses in peripheral blood (Fig. 7f). In addition, analysis of T cell phenotypes revealed elevated frequencies of CD8$^+$ T cells and effector memory T cells in the spleens of the TRAP–mHPV-treated mice compared with controls, indicating the induction of durable T cell immunity (Fig. 7g). Importantly, TRAP-mNV also exhibited a favourable systemic safety profile. Comprehensive haematological, biochemical and histopathological analyses revealed no signs of systemic toxicity following subcutaneous administration (Extended Data Fig. 7a–c).

Discussion

Messenger RNA-based therapies have emerged as a revolutionary tool in precision medicine[2,4,8]. However, mRNA-based cancer vaccines are faced with challenges, including weak immunogenicity and non-specific expression[5,11], particularly in non-lymphatic organs such as the liver[9,12]. In response to this challenge, lymphoid organ-targeted mRNA cancer vaccine delivery strategies offer a promising solution by enhancing immune activation and reducing systemic side effects.

Despite recent advances in utilizing monocytes to deliver poly(β-amino esters)-mRNA particles smaller than one micrometre and screening of cationic lipids or polymers for mRNA delivery to lymphoid organs[13,14,18,19,48,66], these approaches have partially improved delivery efficiency, with inevitable liver accumulation. In contrast, our TRAP strategy, which exploits TfR1 binding for monocyte association, facilitates efficient intracellular mRNA delivery and highly selective LN trafficking, a rare and promising result in the research field. Further in vivo cancer vaccine studies demonstrated robust immune activation and systemic antitumour efficacy using TRAP delivery system. Given

Fig. 7 | Therapeutic efficacy of TRAP–mRNA vaccines on the TC-1 tumour model. a, Time line schematic of TC-1 tumour inoculation (day 0), followed by subcutaneous immunizations with TRAP-mNV formulations on days 5, 8 and 14. **b**, Tumour growth curves of TC-1 tumour-bearing mice treated with PBS, TRAP–mLuc, TRAP–mIL-12, TRAP–mHPV or TRAP–mHPV + mIL-12 formulations (G1–5, colour-coded as per the key beneath the panel). Tumour volume, survival and body weight were monitored throughout the study. **c**, Representative flow cytometry plots showing activated CD8$^+$ T cells (CD3$^+$CD4$^-$CD8$^+$CD69$^+$) in the mouse spleens on day 14 after the first vaccination with the different formulations (G1–5). **d**, Proportion of CD69$^+$CD8$^+$ T cells in the LNs and spleens of the mice in the different vaccination groups. **e**, Representative flow cytometry plots (left) of tetramer staining of splenic CD8$^+$ T cells specific for HPV E7 antigen, gated on CD45$^+$CD3$^+$CD4$^-$CD8$^+$ cells, seven days after the final immunization, with the corresponding quantification (right). **f**, Representative flow cytometry plots (left) and proportion of IFN-γ-producing CD8$^+$ T cells, gated on CD45$^+$CD3$^+$CD4$^-$CD8$^+$ cells, in peripheral blood. **g**, Flow cytometry analysis of memory T cell subsets in the spleen based on CD44 and CD62L expression, gated on CD3$^+$CD8$^+$ cells. T_{EM} cells (CD44$^+$CD62L$^-$) are shown with statistical comparisons. **c**,**e**–**g**, The percentage of cells in the gated regions of interest are shown. **b**,**d**–**g**, Data are presented as the mean ± s.d. Statistical significance was determined using an ordinary one-way ANOVA (two-sided) for all comparisons with the exception of the survival analysis in **b**, where the log-rank Mantel–Cox test was used; exact *P* values are provided; $n = 5$ mice per group. Illustration in **a** created in BioRender: Ren, Q. https://BioRender.com/5ctdmo3 (2026). Source data are provided.

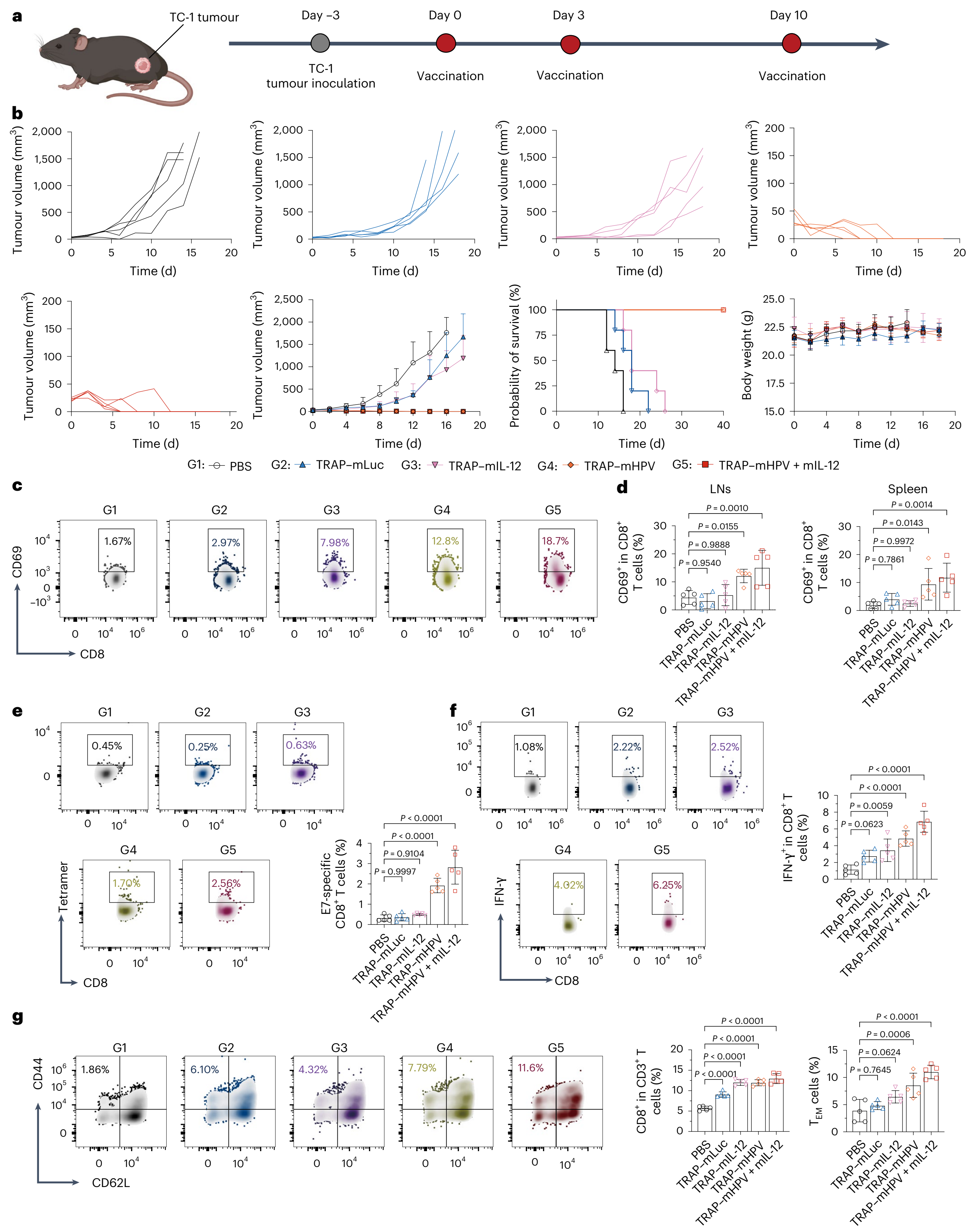
a
TC-1 tumour
Day −3
TC-1
tumour inoculation
Day 0
Vaccination
Day 3
Vaccination
Day 10
Vaccination
b
Tumour volume (mm³)
Time (d)
Probability of survival (%)
Body weight (g)
G1: PBS
G2: TRAP–mLuc
G3: TRAP–mIL-12
G4: TRAP–mHPV
G5: TRAP–mHPV + mIL-12
c
G1 1.67%
G2 2.97%
G3 7.98%
G4 12.8%
G5 18.7%
CD69
CD8
d
LNs
Spleen
CD69⁺ in CD8⁺ T cells (%)
P = 0.0010
P = 0.0155
P = 0.9888
P = 0.9540
P = 0.0014
P = 0.0143
P = 0.9972
P = 0.7861
PBS
TRAP–mLuc
TRAP–mIL-12
TRAP–mHPV
TRAP–mHPV + mIL-12
e
G1 0.45%
G2 0.25%
G3 0.63%
G4 1.70%
G5 2.56%
Tetramer
CD8
E7-specific CD8⁺ T cells (%)
P < 0.0001
P < 0.0001
P = 0.9104
P = 0.9997
f
G1 1.08%
G2 2.22%
G3 2.52%
G4 4.02%
G5 6.25%
IFN-γ
CD8
IFN-γ⁺ in CD8⁺ T cells (%)
P < 0.0001
P < 0.0001
P = 0.0059
P = 0.0623
g
G1 1.86%
G2 6.10%
G3 4.32%
G4 7.79%
G5 11.6%
CD44
CD62L
CD8⁺ in CD3⁺ T cells (%)
P < 0.0001
P < 0.0001
P < 0.0001
P < 0.0001
T_EM cells (%)
P < 0.0001
P = 0.0006
P = 0.0624
P = 0.7645

that TfR1 is expressed in a broad range of cell types, future efforts to improve monocyte-specific vaccine delivery, in the context of systemic administration, may require the use of targeting ligands, such as nanobodies on TRAP, to avoid potential off-target side effects.

It is important to acknowledge several additional limitations of this study. First, we focused on the branched PEI molecule for cyclic disulfide modification because of its lower molecular weight and good safety profile[81,82]. Whether this chemical modification approach could be generalized to other cationic polymers remains unknown. In principle, polymers such as high-molecular-weight PEI, linear PEI, poly(β-amino esters), poly(lactic-co-glycolic acid) and chitosan could also be modified with DTC to achieve targeted mRNA delivery in vivo. Further optimization, including modification of hydrophobic groups or conjugation of targeting ligands, could potentially enhance their mRNA delivery efficiency and organ specificity, respectively. Despite the demonstrated efficacy and safety of the low-molecular-weight branched PEI used in this study, quality control and process development of the molecule to meet regulatory standards might prove to be a challenge due to its polydispersity. More diverse polymers will be included in the future to evaluate the impact of cyclic disulfide modification on mRNA delivery. Second, we assume that cyclic disulfide groups on TRAP would facilitate monocyte association in vivo. Future work should be done to investigate in-depth whether the TRAP particles would have non-specific cellular interactions that could cause potential toxicity issues. Third, these studies were limited to a mouse model. Potential differences in in vivo trafficking of TRAP in larger animals, such as non-human primates, introduce uncertainty when translating findings to human clinical trials.

Despite these limitations, we believe our data provide evidence that TRAP enables precise and efficient mRNA delivery to LNs via a monocyte-driven mechanism. The adaptive immunity activated through this method highlights its potential in immunotherapy and offers a new avenue for the development of clinical cancer vaccines.

Methods

Solvent accessibility analysis of Cys residues

We evaluated the SASA of Cys residues within the extracellular domains of several surface membrane proteins, specifically TfR1 (PDB ID: 1CX8), transferrin-binding protein B (PDB ID: 4O3W), low-density lipoprotein receptor (PDB ID: 1N7D; encompassing β-propeller residues 377–640) and epidermal growth factor receptor (PDB ID: 1IVO). To explore the structural dynamics of TfR1, we performed molecular dynamics simulations where the glycosylated system was prepared using CHARMM-GUI[83] and a reference system without glycosylation was assembled using standard GROMACS[84] procedures. Molecular dynamics systems were constructed based on PDB entry 3KAS, which depicts the receptor in a bound state with another protein and includes glycosylation information. All simulations were performed using the CHARMM36 (refs. 85,86) force field. Each system underwent energy minimization until the maximum force was reduced to <1,000 $\mathrm{kJ^{-1}\,mol^{-1}\,nm^{-1}}$, followed by equilibration under the NVT (constant number of particles, volume and temperature) ensemble using a v-rescale[87] thermostat with a 1 fs time step over 125,000 steps. Subsequently, production runs were conducted with a 2 fs time step, maintaining the temperature at 303.15 K using the v-rescale[87] thermostat and pressure at 1 bar with an isotropic c-rescale[88] barostat. Both Coulombic and van der Waals interactions were truncated at a cutoff distance of 12 Å, and hydrogen bonds were constrained using the LINCS[89] algorithm. Each simulation was extended for 200 ns and three independent replicates were performed for each system to ensure reproducibility. All SASA values were calculated from the simulation trajectories using GROMACS tools. Figures were prepared using Chimera X[90] and VMD[91].

Determination of encapsulation efficiency

The encapsulation efficiency of mRNA was quantified using a Quant-iT RiboGreen RNA assay kit. TRAP–mRNA samples were diluted in 1×TE buffer to assess free mRNA content. A ribosomal RNA standard curve was prepared by serial dilution in the same buffer. Equal volumes of samples or standards were combined with RiboGreen reagent diluted 1:200 in a black, clear-bottom 96-well plate and incubated for 5 min at room temperature. Fluorescence signals were recorded using a microplate reader (excitation, 480 nm; emission, 520 nm). Encapsulation efficiency was calculated as follows: encapsulation efficiency (%) = (fluorescence of total mRNA fluorescence of free mRNA) / (fluorescence of total mRNA) × 100%.

GSH-responsive release assay

To evaluate redox-dependent mRNA release, TRAP–mRNA nanocomplexes were incubated with 10 mM GSH in 1×DPBS or phosphate buffer at 37 °C. Aliquots (200 µl) were withdrawn at designated time points (0–24 h). Released mRNA was quantified using the RiboGreen assay, with fluorescence measured at 480 and 520 nm (excitation and emission, respectively). Cumulative release was calculated from a standard curve and reported as a percentage of the total mRNA loaded.

Cell and animal care

Cell lines were purchased from the Cell Bank of the Chinese Academy of Sciences. L929, B16F10, B16F10-Luc, B16F10-OVA and HEK293T cells were cultured in DMEM medium, and 4T1, LLC, DC2.4, RAW264.7 and Jurkat cells were maintained in RPMI 1640 medium. All media were supplemented with 10% fetal bovine serum and 1% penicillin–streptomycin. All cell lines were confirmed to be mycoplasma-free before use. Cells were cultured at 37 °C in a humidified incubator containing 5% CO_2. Female C57BL/6 mice (6–8 weeks old, approximately 20 g) were obtained from SLAC Laboratory Animal Co., Ltd, and female Ai9 mice (6–8 weeks old, approximately 20 g) were obtained from Suzhou Abogen Biosciences. All animals were maintained under specific-pathogen-free conditions at Soochow University with ad libitum access to food and water. The mice were housed in climate-controlled rooms under a 12 h light–dark cycle with 40–70% relative humidity and acclimated for at least one week before random assignment into experimental groups. All animal procedures were approved by the Ethics Committee of Soochow University (approval number SUDA20240716A03) and were conducted in accordance with institutional guidelines for the care and use of laboratory animals.

Synthesis of TRAP

Dithiolane trimethylene carbonate and PEI were mixed at a molar ratio of 15:1 (DTC:PEI) and dissolved in dimethylsulfoxide to a concentration of 300 mg $\mathrm{ml^{-1}}$. Polymerization was performed at room temperature under stirring for 48 h. The resulting polymer was purified by dialysis against dimethylsulfoxide (three cycles, 24 h each), precipitated with anhydrous ethanol, re-dissolved in anhydrous tetrahydrofuran and re-precipitated with anhydrous ethyl ether. The product was washed twice, vacuum-dried for 48 h and stored for further use.

Preparation of TRAP–mRNA

Messenger RNA was dissolved in 10 mM HEPES buffer (pH 5.2), and TRAP was prepared in 100 mM sodium acetate buffer (pH 4.0). The TRAP and mRNA were combined at a fixed mass ratio of 6:1 by rapid mixing to generate cationic nanocomplexes, which were stored at 4 °C until use. The hydrodynamic diameter, polydispersity index and zeta potential were determined using a Zetasizer Nano ZS90 system (Malvern). Particle morphology was examined by transmission electron microscopy (HT7700, 120 kV) using copper grids.

Sequences of mRNA

The mouse mRNA constructs used in this study were synthesized by Catug Biotechnology Co., Ltd according to the specified coding sequences. The mRNA coding sequences are provided in Supplementary Data 1. All newly generated mRNA are available for reuse on reasonable request; requests should be directed to the corresponding authors.

Thiol-mediated cellular uptake

Cellular uptake of TRAP was visualized by confocal microscopy. Cell nuclei were stained with Hoechst 33342, and Cy5-labelled TRAP-mNV was imaged at the indicated time points. Lysosomal co-localization was examined using stimulated emission depletion confocal microscopy. Nanoparticles assembled from nTRAP and mRNA were analysed in parallel under identical conditions. *Z*-stack imaging was performed to enable accurate three-dimensional assessment of lysosomal localization. To investigate uptake mechanisms, DC2.4 cells were pretreated with endocytosis inhibitors—dynasore, chlorpromazine or DTNB—for 2 h before incubation with Cy5-labelled TRAP-mNV for 1 or 6 h. For transferrin receptor involvement, cells were pretreated with ferristatin II for 4–8 h before exposure to TRAP-mNV. The cells were then collected and analysed by flow cytometry (BD LSRFortessa) and data were processed using FlowJo (v10).

Assessment of intracellular mRNA delivery efficiency

DC2.4 and RAW264.7 cells were seeded in 24-well plates at a density of 1×10^5 cells per well and incubated for 12 h. The cells were then treated with TRAP, Lipofectamine 2000 or Lipofectamine MessengerMAX for 4 h, followed by replacement with fresh complete medium and further incubation for 24 h. The cells were subsequently collected and EGFP expression was analysed by flow cytometry.

Immunoprecipitation and immunoblotting

Strep-Tactin magnetic beads (Smart-Lifesciences) were preloaded with biotin-DTC by incubation at 4 °C for 3 h. HEK293T cells expressing Flag–GFP, Flag–transferrin or Flag–TfR1 were harvested and lysed (on ice for 10 min) in lysis buffer (20 mM Tris–HCl pH 7.4, 2 mM EDTA, 25 mM NaF and 1% Triton X-100) supplemented with protease inhibitors (Sigma). The lysates were clarified by centrifugation at 12,000*g* for 10 min and the protein concentrations were determined. Equal amounts of lysates were incubated with the pretreated beads for 1 h at 4 °C. After three washes with wash buffer (50 mM Tris–HCl pH 8.0, 150 mM NaCl, 1% NP-40, 0.5% sodium deoxycholate and 0.1% SDS), the bound proteins were eluted by boiling the samples in SDS sample buffer at 95 °C for 5 min. The eluted proteins were resolved by SDS–PAGE, transferred onto a polyvinylidene fluoride membrane and subjected to immunoblot analysis. Immunoblotting was performed using the indicated primary antibodies and horseradish peroxidase-conjugated secondary antibodies, followed by chemiluminescent detection. Antibodies to Flag (M2), STING, phospho-STING (Ser365), IRF3, phospho-IRF3 (Ser396), TBK1, phospho-TBK1 (Ser172) and β-tubulin were used.

Flow cytometry

After processing, cells were stained for viability using anti-zombie NIR (APC/Cy7 viability dye). The staining was performed for 30 min at 4 °C, followed by washing with FACS buffer (1×PBS containing 0.2% bovine serum albumin and 1 mM EDTA). The cells were then incubated with Fc block (FACS buffer containing anti-CD16/32) at 4 °C for 30 min to prevent non-specific binding. Tetramer-specific $CD8^+$ T cells were identified by staining with SIINFEKL-MHC-I tetramers in 50 µl FACS buffer for 35–45 min at 4 °C. Surface marker staining was subsequently performed in 50 µl FACS buffer at 4 °C for 20–25 min, followed by washing before acquisition. For the transcription factor analysis, the cells were first surface-stained, as described earlier, and then fixed and permeabilized using an eBioscience Foxp3 transcription factor fixation/permeabilization kit for 30 min at 4 °C. The cells were washed with permeabilization buffer and incubated with transcription factor antibodies in 1×permeabilization buffer for 1 h at 4 °C. After the final washes, the cells were resuspended in FACS buffer and analysed by flow cytometry.

Monocyte differentiation assay

Mice were subcutaneously injected at the tail base with Cy5-labelled TRAP–mRNA complexes (10 µg mRNA in 100 µl). At 0, 1, 3 and 8 h post injection, tissue from the injection site was collected, enzymatically digested and processed into single-cell suspensions for flow cytometry. Cy5 fluorescence was analysed in $CD45^+$ (immune) and $CD45^-$ (non-immune) cells to assess mRNA uptake. $CD45^+CD11b^+$ myeloid cells were further characterized for uptake and differentiated into $Ly6C^+$ monocytes, $CD11c^+$ DCs and $F4/80^+$ macrophages. The dynamics of $Ly6C^+CD11c^+$ cells and XCR1 expression on $Ly6C^+$ monocytes were evaluated over time.

Analysis of myeloid cell dynamics

To investigate the kinetics and cellular specificity of TRAP-mediated mRNA delivery and translation, we employed *Cre* mRNA (for recombination-based lineage tracing) in Ai9 mice and *Thy1.1* mRNA (membrane-anchored reporter) in wild-type C57BL/6 mice. For LN analysis, the mice were subcutaneously injected at the tail base with TRAP-formulated *Cre* mRNA (10 µg) or *Thy1.1* mRNA, and their LNs were harvested 3, 12 and 24 h post injection. Single-cell suspensions were prepared and stained for CD11b, CD11c, Ly6C, F4/80 and other relevant markers. For the Ai9 mice, *Cre*-mediated recombination was assessed by tdTomato expression in DCs, macrophages and monocytes. For the Thy1.1 experiments, Thy1.1 expression served as a surrogate for mRNA translation in the myeloid subsets. For the injection-site analysis, skin tissues surrounding the tail base were collected 3, 12 and 24 h following subcutaneous injection of TRAP–mThy1.1. The tissue was minced and enzymatically digested into single-cell suspensions for flow cytometry. $CD11b^+$ myeloid cells were gated and further classified into DCs ($CD11c^+$), macrophages ($F4/80^+$) and monocytes ($Ly6C^+$). The $Thy1.1^+$ cells in each subpopulation were quantified to assess the efficiency of in situ translation. Flow cytometry was performed using a Beckman Coulter CytoFLEX system and analysed using the FlowJo software.

In vivo imaging system imaging

C57BL/6 mice ($n = 5$–6 per group) were injected with PBS, LNP or TRAP (TRAP–mLuc; 10 µg mLuc per mouse) at the tail base. LNPs were formulated using SM-102, DSPC, cholesterol and PEG-lipid, all of which were purchased from AVT (Shanghai) Pharmaceutical Tech Co., Ltd. Six hours post injection, D-luciferin potassium salt (150 mg kg^{-1}) was administered intraperitoneally. After 10 min, the mice were euthanized and the inguinal LNs, along with other major organs, were collected. The harvested tissues were then subjected to imaging using an in vivo imaging system (IVIS) to assess firefly Luc expression and biodistribution.

Macrophage depletion

To deplete macrophages in vivo, mice were intraperitoneally administered a 200-µl dose of CL-lipo (catalog no. 40337; Yeasen, Shanghai, China) on day 0, followed by a second dose of 100 µl on day 4. Control mice received equal volumes of PBS containing control liposomes. The mice were euthanized on day 5 and immune cells from peripheral blood, peritoneal lavage fluid, spleen and draining LNs were collected for analysis. Cell populations were analysed by flow cytometry using the markers CD11b, CD11c, Ly6C and F4/80 to distinguish DCs, macrophages and monocytes.

Mechanistic analysis of lymph node targeting

To investigate the mechanism of LN targeting, $CD11b^+$ myeloid cells in LN sections were stained 6 h after caudal basal subcutaneous administration of Cy5-labelled TRAP to observe their co-localization. Simultaneously, vascular migration of the TRAP was analysed by staining blood vessels with anti-CD31. Dextran–FITC was intravenously administered to C57BL/6 mice via the tail vein 1 h after subcutaneous administration of Cy5-labelled TRAP–mRNA. Three-dimensional reconstruction of the intravascular nanoparticle migration was performed using the Imaris Viewer software. For in vivo antibody blocking studies, 100 µg anti-CD62L (clone Mel-14, BioXCell) and/or 100 µg anti-PSGL-1 (clone 4RA10, BioXCell) were administered intraperitoneally at the time of immunization and subsequently daily for up to three days.

Detection of cytosolic mitochondrial DNA

RAW264.7 cells and BMDCs were incubated with TRAP for 6 h and then divided into two equal fractions. One fraction was resuspended in PBS for total DNA analysis. The other fraction was lysed in Buffer A (10 mM Tris–HCl pH 7.5, 10 mM KCl, 1.5 mM $MgCl_2$ and 0.25 M D-mannitol, supplemented with protease inhibitors) and gently mixed for 30 min at 4 °C for cytosolic extraction. The lysates were centrifuged at 700*g* for 10 min, and the supernatant was further cleared by centrifugation at 15,000*g* and 4 °C for 30 min to obtain cytosolic fractions. DNA from the cytosolic fractions and total cell lysates was purified using DNeasy mini spin columns (QIAGEN) and quantified by quantitative PCR using the following primer pairs targeting nuclear DNA (Tert) and mtDNA (D-loop): mtDNA D-loop forward, 5′-AATCTACCATCCTCCGTGAAACC-3′ and mtDNA D-loop reverse, 5′-TCAGTTTAGCTACCCCCAAGTTTAA-3′; nucDNA Tert forward, 5′-CTAGCTCATGTGTCAAGACCCTCTT-3′ and nucDNA Tert reverse, 5′-GCCAGCACGTTTCTCTCGTT-3′. The cytosolic mtDNA levels were normalized to the total cellular mtDNA based on the Tert C_t values and expressed as percentages. The absence of Tert amplification in the cytosolic samples confirmed minimal nuclear contamination.

Assessment of in vivo immune-cell uptake and responses

C57BL/6 mice were anaesthetized and subcutaneously injected with 50 µl TRAP formulated with Cy5-labelled mRNA. The mice were euthanized 0.5, 1.0 and 3.0 h following injection, and skin tissue at the injection site and inguinal LNs were collected. The skin tissue was minced and enzymatically digested with 2 mg ml^{-1} collagenase D at 37 °C for 1 h. Single-cell suspensions were prepared by sequential filtration (50 µm and then 40 µm), followed by red-blood-cell lysis with ACK buffer. The cells were washed, blocked with anti-CD16/32 and stained with the indicated antibody panels. At later time points (6, 12, 24 and 36 h), LNs were processed similarly and stained with antibodies to CD64, Ly6C, CD11b and CD11c. After washing, the cells were analysed by flow cytometry.

In vivo immunogenicity study

Different formulations were subcutaneously injected into the tail base of C57BL/6 mice, and the activation and antigen presentation of DCS in inguinal LNs of mice were detected on day 3. In addition, C57BL/6 mice were immunized with TRAP–mOVA and TRAP–mOVA + mIL-12. Spleens from both sets of experiments were harvested on day 14. The number of Ag-specific T cells (IFN-γ) in the spleen was determined using an ELISpot assay. Splenocytes were seeded in 96-well plates (1×10^5 cells per well) precoated with mouse anti-IFN-γ as per the manufacturer's instructions. The splenocytes were stimulated with 25 µg ml^{-1} OVA for 24 h. A biotinylated antibody specific for IFN-γ and alkaline phosphatase conjugated to streptavidin were subsequently used to detect the secreted IFN-γ. Splenocytes were also plated in 24-well plates (2×10^6 per well) and pulsed with OVA. After 72 h, the cells were centrifuged and washed with FACS buffer, incubated with anti-CD16/32 at room temperature, and then stained with antibodies to CD3, CD8 and IFN-γ. The cells were then washed twice with FACS buffer and analysed using a flow cytometer. The cytokine levels in the serum and LNs were measured using a LEGENDplex MU inflammation panel (13-plex) with VbP.

In vivo tumour therapy

For therapeutic efficacy evaluation, C57BL/6 mice were subcutaneously inoculated with 2×10^5 B16F10-OVA cells on both the left and right flanks on day 0. The mice were immunized with nanoparticle vaccines on days 5, 8 and 14. In the B16F10 tumour treatment model, the mice were subcutaneously injected with 2 µg mIL-12 and 10 µg mOVA per dose. *Luc* mRNA was administered as an isotype control. In addition, intratumoral injections of IL-12 into the primary tumour on the left flank were performed following a clinical strategy to serve as a comparison. The potential of co-delivering antigen and mIL-12 to stimulate systemic immune responses was assessed by examining the inhibition of both primary and secondary tumour growth across varying doses of treatment. For the TC-1 tumour model, C57BL/6 mice were subcutaneously inoculated with 5×10^5 TC-1 cells on the right flank on day 3. The mice were subcutaneously vaccinated with TRAP–mHPV formulations on days 0, 3 and 10 according to the same immunization schedule used in the B16F10 model. For metastasis modelling, C57BL/6 mice were intravenously inoculated with 5×10^5 B16F10-Luc cells on day 0 and immunized with TRAP on days 3, 6, 9 and 16. D-Luciferin potassium salt (150 mg kg^{-1}) was administered intraperitoneally. After 10 min, the mice were imaged using an in vivo imaging system to assess firefly Luc expression and biodistribution. Caliper measurements were made and the subcutaneous tumour volume was estimated using the formula $(\text{width}^2 \times \text{length}) / 2$. The maximum tumour burden permitted by the ethics committee was 2,000 mm^3; this limit was not exceeded at any point during the study.

Statement

No statistical methods were used to pre-determine sample sizes but our sample sizes are similar to those reported in previous publications[92]. The investigators were not blinded to allocation during data acquisition or analysis, as measurements were obtained using the same instrumentation and did not involve subjective scoring. Data distribution was assumed to be normal but this was not formally tested; individual data points are shown where applicable. Animals were randomly assigned to experimental groups and no additional blocking or randomization of experimental conditions was applied. No animals or data points were excluded from the final analyses.

Statistical analysis and reproducibility

Statistical analyses were performed using GraphPad Prism v.10 and all quantitative data are presented as the mean ± s.d. Comparisons between two groups were conducted using an unpaired two-sided Student's *t*-test, whereas comparisons among more than two groups were analysed using a one-way or two-way ANOVA, followed by Tukey's multiple comparisons test. $P > 0.05$ was considered not significant. At least three biological replicates were analysed for all quantitative experiments. The transmission electron microscopy, CLSM, haematoxylin and eosin staining, immunofluorescence and immunohistochemistry experiments were repeated at least three independent times with similar results.

Reporting summary

Further information on research design is available in the Nature Portfolio Reporting Summary linked to this article.

Data availability

All data supporting the findings of this study are available within the Article, Supplementary Information and Source Data. Source data are provided with this paper. Additional data are available from the corresponding authors on reasonable request.

References

1. Chaudhary, N., Weissman, D. & Whitehead, K. A. mRNA vaccines for infectious diseases: principles, delivery and clinical translation. *Nat. Rev. Drug Discov.* **20**, 817–838 (2021).
2. Edwards, D. K. & Carfi, A. Messenger ribonucleic acid vaccines against infectious diseases: current concepts and future prospects. *Curr. Opin. Immunol.* **77**, 102214 (2022).

3. Pardi, N., Hogan, M. J., Porter, F. W. & Weissman, D. mRNA vaccines—a new era in vaccinology. *Nat. Rev. Drug Discov.* **17**, 261–279 (2018).
4. Zhang, G., Tang, T., Chen, Y., Huang, X. & Liang, T. mRNA vaccines in disease prevention and treatment. *Signal Transduct. Target. Ther.* **8**, 365 (2023).
5. Bitounis, D., Jacquinet, E., Rogers, M. A. & Amiji, M. M. Strategies to reduce the risks of mRNA drug and vaccine toxicity. *Nat. Rev. Drug Discov.* **23**, 281–300 (2024).
6. Kon, E., Ad-El, N., Hazan-Halevy, I., Stotsky-Oterin, L. & Peer, D. Targeting cancer with mRNA–lipid nanoparticles: key considerations and future prospects. *Nat. Rev. Clin. Oncol.* **20**, 739–754 (2023).
7. Xia, Y., Fu, S., Ma, Q., Liu, Y. & Zhang, N. Application of nano-delivery systems in lymph nodes for tumor immunotherapy. *Nanomicro Lett.* **15**, 145 (2023).
8. Aldén, M. et al. Intracellular reverse transcription of Pfizer BioNTech COVID-19 mRNA vaccine BNT162b2 in vitro in human liver cell line. *Curr. Issues Mol. Biol.* **44**, 1115–1126 (2022).
9. Boettler, T. et al. SARS-CoV-2 vaccination can elicit a CD8 T-cell dominant hepatitis. *J. Hepatol.* **77**, 653–659 (2022).
10. Loughrey, D. & Dahlman, J. E. Non-liver mRNA delivery. *Acc. Chem. Res.* **55**, 13–23 (2022).
11. Cosentino, M. & Marino, F. The spike hypothesis in vaccine-induced adverse effects: questions and answers. *Trends Mol. Med.* **28**, 797–799 (2022).
12. Trougakos, I. P. et al. Adverse effects of COVID-19 mRNA vaccines: the spike hypothesis. *Trends Mol. Med.* **28**, 542–554 (2022).
13. Chen, J. et al. Lipid nanoparticle-mediated lymph node-targeting delivery of mRNA cancer vaccine elicits robust CD8$^+$ T cell response. *Proc. Natl Acad. Sci. USA* **119**, e2207841119 (2022).
14. Han, X. et al. Adjuvant lipidoid-substituted lipid nanoparticles augment the immunogenicity of SARS-CoV-2 mRNA vaccines. *Nat. Nanotechnol.* **18**, 1105–1114 (2023).
15. Liu, M. et al. Lymph-targeted high-density lipoprotein-mimetic nanovaccine for multi-antigenic personalized cancer immunotherapy. *Sci. Adv.* **10**, eadk2444 (2024).
16. Wang, S. et al. Macrophage-tumor chimeric exosomes accumulate in lymph node and tumor to activate the immune response and the tumor microenvironment. *Sci. Transl. Med.* **13**, eabb6981 (2021).
17. Li, Y. et al. Rapid surface display of mRNA antigens by bacteria-derived outer membrane vesicles for a personalized tumor vaccine. *Adv. Mater.* **34**, e2109984 (2022).
18. Zhang, D. et al. Targeted delivery of mRNA with one-component ionizable amphiphilic Janus dendrimers. *J. Am. Chem. Soc.* **143**, 17975–17982 (2021).
19. Zhang, D. et al. The unexpected importance of the primary structure of the hydrophobic part of one-component ionizable amphiphilic Janus dendrimers in targeted mRNA delivery activity. *J. Am. Chem. Soc.* **144**, 4746–4753 (2022).
20. Jiang, H., Wang, Q. & Sun, X. Lymph node targeting strategies to improve vaccination efficacy. *J. Control. Release* **267**, 47–56 (2017).
21. Lei, J. et al. Development of mannosylated lipid nanoparticles for mRNA cancer vaccine with high antigen presentation efficiency and immunomodulatory capability. *Angew. Chem. Int. Ed.* **63**, e202318515 (2024).
22. Zhou, L. et al. Tumor cell-released kynurenine biases MEP differentiation into megakaryocytes in individuals with cancer by activating AhR–RUNX1. *Nat. Immunol.* **24**, 2042–2052 (2023).
23. Zhu, L. et al. Microbiota-assisted iron uptake promotes immune tolerance in the intestine. *Nat. Commun.* **14**, 2790 (2023).
24. Hansen, F. J. et al. CD71 expressing circulating neutrophils serve as a novel prognostic biomarker for metastatic spread and reduced outcome in pancreatic ductal adenocarcinoma patients. *Sci. Rep.* **14**, 21164 (2024).
25. Candelaria, P. V., Leoh, L. S., Penichet, M. L. & Daniels-Wells, T. R. Antibodies targeting the transferrin receptor 1 (TfR1) as direct anti-cancer agents. *Front. Immunol.* **12**, 607692 (2021).
26. Daniels, T. R., Delgado, T., Rodriguez, J. A., Helguera, G. & Penichet, M. L. The transferrin receptor part I: biology and targeting with cytotoxic antibodies for the treatment of cancer. *Clin. Immunol.* **121**, 144–158 (2006).
27. Zhang, D. et al. Transferrin receptor targeting chimeras for membrane protein degradation. *Nature* **638**, 787–795 (2025).
28. Baeyens, A. et al. Monocyte-derived S1P in the lymph node regulates immune responses. *Nature* **592**, 290–295 (2021).
29. Chen, K. Y. et al. Inflammation switches the chemoattractant requirements for naive lymphocyte entry into lymph nodes. *Cell* **188**, 1019–1035 (2024).
30. Elewaut, A. et al. Cancer cells impair monocyte-mediated T cell stimulation to evade immunity. *Nature* **637**, 716–725 (2024).
31. Langlet, C. et al. CD64 expression distinguishes monocyte-derived and conventional dendritic cells and reveals their distinct role during intramuscular immunization. *J. Immunol.* **188**, 1751–1760 (2012).
32. León, B., López-Bravo, M. & Ardavín, C. Monocyte-derived dendritic cells formed at the infection site control the induction of protective T helper 1 responses against Leishmania. *Immunity* **26**, 519–531 (2007).
33. Zhang, F. et al. Genetic programming of macrophages to perform anti-tumor functions using targeted mRNA nanocarriers. *Nat. Commun.* **10**, 3974 (2019).
34. Kang, M. et al. Nanocomplex-mediated in vivo programming to chimeric antigen receptor–M1 macrophages for cancer therapy. *Adv. Mater.* **33**, e2103258 (2021).
35. Tang, Y. et al. Precise delivery of nanomedicines to M2 macrophages by combining 'eat me/don't eat me' signals and its anticancer application. *ACS Nano* **15**, 18100–18112 (2021).
36. Graversen, J. H. et al. Targeting the hemoglobin scavenger receptor CD163 in macrophages highly increases the anti-inflammatory potency of dexamethasone. *Mol. Ther.* **20**, 1550–1558 (2012).
37. Zheng, L. et al. In vivo monocyte/macrophage-hitchhiked intratumoral accumulation of nanomedicines for enhanced tumor therapy. *J. Am. Chem. Soc.* **142**, 382–391 (2020).
38. Liu, C., Shang, C., Ma, L., Zhou, X. & Guo, C. Abstract 377: Evaluating delivery of TFR1-targeting therapies to the CNS in a novel humanized TFR1 mouse model. *Cancer Res.* **82**, 377–377 (2022).
39. Cheng, Y., Zak, O., Aisen, P., Harrison, S. C. & Walz, T. Structure of the human transferrin receptor–transferrin complex. *Cell* **116**, 565–576 (2004).
40. Lebrón, J. A. et al. Crystal structure of the hemochromatosis protein HFE and characterization of its interaction with transferrin receptor. *Cell* **93**, 111–123 (1998).
41. Abraham, J., Corbett, K. D., Farzan, M., Choe, H. & Harrison, S. C. Structural basis for receptor recognition by New World hemorrhagic fever arenaviruses. *Nat. Struct. Mol. Biol.* **17**, 438–444 (2010).
42. Gruszczyk, J. et al. Cryo-EM structure of an essential *Plasmodium vivax* invasion complex. *Nature* **559**, 135–139 (2018).
43. Choi, Y. S. et al. Beyond hydrophilic polymers in amphiphilic polymer-based self-assembled NanoCarriers: small hydrophilic carboxylate-capped disulfide drug delivery system and its multifunctionality and multispatial targetability. *Biomaterials* **280**, 121307 (2022).
44. Zhang, P. et al. Systemic multifunctional nanovaccines for potent personalized immunotherapy of acute myeloid leukemia. *Adv. Mater.* **36**, e2407189 (2024).

45. Qu, L. et al. A biomimetic autophagosomes-based nanovaccine boosts anticancer immunity. *Adv. Mater.* **36**, e2409590 (2024).
46. Kong, H. et al. An antifouling membrane-fusogenic liposome for effective intracellular delivery in vivo. *Nat. Commun.* **15**, 4267 (2024).
47. Brown, D. W. et al. Safe and effective in vivo delivery of DNA and RNA using proteolipid vehicles. *Cell* **187**, 5357–5375 (2024).
48. Zhao, C., Wang, C., Shan, W., Wang, W. & Deng, H. Fusogenic lipid nanovesicle for biomacromolecular delivery. *Nano Lett.* **24**, 8609–8618 (2024).
49. Zhuo, Y. et al. Direct cytosolic delivery of siRNA via cell membrane fusion using cholesterol-enriched exosomes. *Nat. Nanotechnol.* **19**, 1858–1868 (2024).
50. Laurent, Q. et al. Thiol-mediated uptake. *JACS Au* **1**, 710–728 (2021).
51. Du, S., Liew, S. S., Li, L. & Yao, S. Q. Bypassing endocytosis: direct cytosolic delivery of proteins. *J. Am. Chem. Soc.* **140**, 15986–15996 (2018).
52. Derakhshankhah, H. & Jafari, S. Cell penetrating peptides: a concise review with emphasis on biomedical applications. *Biomed. Pharmacother.* **108**, 1090–1096 (2018).
53. Guo, J. et al. Rational design of poly(disulfide)s as a universal platform for delivery of CRISPR–Cas9 machineries toward therapeutic genome editing. *ACS Cent. Sci.* **7**, 990–1000 (2021).
54. Shu, Z. et al. Disulfide-unit conjugation enables ultrafast cytosolic internalization of antisense DNA and siRNA. *Angew. Chem. Int. Ed.* **58**, 6611–6615 (2019).
55. Martinent, R. et al. Dithiolane quartets: thiol-mediated uptake enables cytosolic delivery in deep tissue. *Chem. Sci.* **12**, 13922–13929 (2021).
56. Abegg, D. et al. Strained cyclic disulfides enable cellular uptake by reacting with the transferrin receptor. *J. Am. Chem. Soc.* **139**, 231–238 (2017).
57. Kanjilal, P., Dutta, K. & Thayumanavan, S. Thiol-disulfide exchange as a route for endosomal escape of polymeric nanoparticles. *Angew. Chem. Int. Ed.* **61**, e202209227 (2022).
58. Cai, T., Liu, H., Zhang, S., Hu, J. & Zhang, L. Delivery of nanovaccine towards lymphoid organs: recent strategies in enhancing cancer immunotherapy. *J. Nanobiotechnol.* **19**, 389 (2021).
59. Najibi, A. J. & Mooney, D. J. Cell and tissue engineering in lymph nodes for cancer immunotherapy. *Adv. Drug Deliv. Rev.* **161–162**, 42–62 (2020).
60. Wang, Q. et al. Lymph node-targeting nanovaccines for cancer immunotherapy. *J. Control. Release* **351**, 102–122 (2022).
61. Wauters, A. C. et al. Polymersomes with splenic avidity target red pulp myeloid cells for cancer immunotherapy. *Nat. Nanotechnol.* **19**, 1735–1744 (2024).
62. Griffith, J. W., Sokol, C. L. & Luster, A. D. Chemokines and chemokine receptors: positioning cells for host defense and immunity. *Annu. Rev. Immunol.* **32**, 659–702 (2014).
63. Murdoch, C. & Finn, A. Chemokine receptors and their role in inflammation and infectious diseases. *Blood* **95**, 3032–3043 (2000).
64. Leal, J. M. et al. Innate cell microenvironments in lymph nodes shape the generation of T cell responses during type I inflammation. *Sci. Immunol.* **6**, eabb9435 (2021).
65. Drakesmith, H. et al. The hemochromatosis protein HFE inhibits iron export from macrophages. *Proc. Natl Acad. Sci. USA* **99**, 15602–15607 (2002).
66. Hu, Y. Z. et al. Supramolecular assembly of polycation/mRNA nanoparticles and in vivo monocyte programming. *Proc. Natl Acad. Sci. USA* **121**, e2400194121 (2024).
67. Cheong, C. et al. Microbial stimulation fully differentiates monocytes to DC-SIGN/CD209$^+$ dendritic cells for immune T cell areas. *Cell* **143**, 416–429 (2010).
68. Menezes, S. et al. The heterogeneity of Ly6C^{hi} monocytes controls their differentiation into iNOS$^+$ macrophages or monocyte-derived dendritic cells. *Immunity* **45**, 1205–1218 (2016).
69. Zigmond, E. et al. Ly6C^{hi} monocytes in the inflamed colon give rise to proinflammatory effector cells and migratory antigen-presenting cells. *Immunity* **37**, 1076–1090 (2012).
70. Yona, S. et al. Fate mapping reveals origins and dynamics of monocytes and tissue macrophages under homeostasis. *Immunity* **38**, 79–91 (2013).
71. Elsner, R. A., Smita, S. & Shlomchik, M. J. IL-12 induces a B cell-intrinsic IL-12/IFNγ feed-forward loop promoting extrafollicular B cell responses. *Nat. Immunol.* **25**, 1283–1295 (2024).
72. Li, C. et al. Mechanisms of innate and adaptive immunity to the Pfizer-BioNTech BNT162b2 vaccine. *Nat. Immunol.* **23**, 543–555 (2022).
73. Garcia, E. & Ismail, S. Spatiotemporal regulation of signaling: focus on T cell activation and the immunological synapse. *Int. J. Mol. Sci.* **21**, 3283 (2020).
74. Hashimoto, M., Im, S. J., Araki, K. & Ahmed, R. Cytokine-mediated regulation of CD8 T-cell responses during acute and chronic viral infection. *Cold Spring Harb. Perspect. Biol.* **11**, a028464 (2019).
75. Brunner, P., Kiwitz, L., Li, L. & Thurley, K. Diffusion-limited cytokine signaling in T cell populations. *iScience* **27**, 110134 (2024).
76. Sterner, R. M. et al. GM-CSF inhibition reduces cytokine release syndrome and neuroinflammation but enhances CAR-T cell function in xenografts. *Blood* **133**, 697–709 (2019).
77. Zhang, C., Wu, Z., Li, J. W., Zhao, H. & Wang, G. Q. Cytokine release syndrome in severe COVID-19: interleukin-6 receptor antagonist tocilizumab may be the key to reduce mortality. *Int. J. Antimicrob. Agents* **55**, 105954 (2020).
78. Dempsey, L. A. Immunoregulatory itaconate. *Nat. Immunol.* **19**, 511 (2018).
79. Villar, J. & Segura, E. The more, the merrier: DC3s join the human dendritic cell family. *Immunity* **53**, 233–235 (2020).
80. Terashima, A. et al. Sepsis-induced osteoblast ablation causes immunodeficiency. *Immunity* **44**, 1434–1443 (2016).
81. Godbey, W. T., Wu, K. K. & Mikos, A. G. Poly(ethylenimine) and its role in gene delivery. *J. Control. Release* **60**, 149–160 (1999).
82. Kunath, K. et al. Low-molecular-weight polyethylenimine as a non-viral vector for DNA delivery: comparison of physicochemical properties, transfection efficiency and in vivo distribution with high-molecular-weight polyethylenimine. *J. Control. Release* **89**, 113–125 (2003).
83. Lee, J. et al. CHARMM-GUI input generator for NAMD, GROMACS, AMBER, OpenMM, and CHARMM/OpenMM simulations using the CHARMM36 additive force field. *J. Chem. Theory Comput.* **12**, 405–413 (2016).
84. Abraham, M. J. et al. GROMACS: high performance molecular simulations through multi-level parallelism from laptops to supercomputers. *SoftwareX* **1–2**, 19–25 (2015).
85. Best, R. B. et al. Optimization of the additive CHARMM all-atom protein force field targeting improved sampling of the backbone φ, ψ and side-chain χ_1 and χ_2 dihedral angles. *J. Chem. Theory Comput.* **8**, 3257–3273 (2012).
86. Huang, J. et al. CHARMM36m: an improved force field for folded and intrinsically disordered proteins. *Nat. Methods* **14**, 71–73 (2017).
87. Bussi, G., Zykova-Timan, T. & Parrinello, M. Isothermal-isobaric molecular dynamics using stochastic velocity rescaling. *J. Chem. Phys.* **130**, 074101 (2009).

88. Bernetti, M. & Bussi, G. Pressure control using stochastic cell rescaling. *J. Chem. Phys.* **153**, 114107 (2020).
89. Hess, B., Bekker, H., Berendsen, H. J. C. & Fraaije, J. G. E. M. LINCS: a linear constraint solver for molecular simulations. *J. Comput. Chem.* **18**, 1463–1472 (1997).
90. Goddard, T. D. et al. UCSF ChimeraX: meeting modern challenges in visualization and analysis. *Protein Sci.* **27**, 14–25 (2018).
91. Humphrey, W., Dalke, A. & Schulten, K. VMD: visual molecular dynamics. *J. Mol. Graph.* **14**, 33–38 (1996).
92. Li, L. et al. Burst release of encapsulated annexin A5 in tumours boosts cytotoxic T-cell responses by blocking the phagocytosis of apoptotic cells. *Nat. Biomed. Eng.* **4**, 1102–1116 (2020).

Acknowledgements

We acknowledge financial support from National Natural Science Foundation of China (grant numbers U25A20260 and 52233007), Jiangsu Provincial Department of Science and Technology (grant numbers BG2025060 and BG2025053), Natural Science Foundation of Jiangsu Province (grant number SBK20250405084). We thank L. Wang and J. Yang for synthesizing mRNA, and J. Zhu for assistance in the preliminary cell experiments. The funders had no role in study design, data collection and analysis, decision to publish or preparation of the manuscript.

Author contributions

Q.R., X.Z. and L.Z. performed experiments, analysed data and wrote the manuscript. R.Y., L.C., K.R., X.P., Y.Z., Y.Q., K.C.C., L.C., L.D. and P.G. assisted with the preparation of reagents, data analysis and manuscript preparation. Z.Z., C.X., F.Z., C.D., B.Y. and F.M. conceptualized the project, designed and supervised the research, and wrote the manuscript.

Competing interests

Z.Z., C.X., R.Y., Q.R. and F.M. have filed a provisional patent (China, CN202510375982.0) related to DTC-modified PEI for mRNA delivery, which is relevant to the mRNA delivery platform investigated in this study. K.R. is a co-founder of Catug Biotechnology Co., Ltd, and X.P. is an employee of Catug Biotechnology Co., Ltd, which is involved in the synthesis of mRNA used in this work. B.Y. is the founder of Suzhou Abogen Biosciences, and L.D. and P.G. are employees of Suzhou Abogen Biosciences. The other authors declare no competing interests.

Additional information

Extended data is available for this paper at https://doi.org/10.1038/s41551-026-01672-0.

Supplementary information The online version contains supplementary material available at https://doi.org/10.1038/s41551-026-01672-0.

Correspondence and requests for materials should be addressed to Fangfang Zhou, Congcong Xu or Zhiyuan Zhong.

Peer review information *Nature Biomedical Engineering* thanks Lin Mei, Xianzhu Yang and the other, anonymous, reviewer(s) for their contribution to the peer review of this work. Peer reviewer reports are available.

Reprints and permissions information is available at www.nature.com/reprints.

---

[1]Biomedical Polymers Laboratory, College of Chemistry, Chemical Engineering and Materials Science, Soochow University, Suzhou, P. R. China. [2]Institutes of Biology and Medical Science, Soochow University, Suzhou, P. R. China. [3]Catug Biotechnology Co. Ltd, Suzhou, P. R. China. [4]Department of Biosciences and Bioinformatics, School of Science, Xi'an Jiaotong–Liverpool University, Suzhou, P. R. China. [5]School of Pharmacy, Shanghai Jiao Tong University, Shanghai, P. R. China. [6]College of Pharmaceutical Sciences, Soochow University, Suzhou, P. R. China. [7]Suzhou Abogen Biosciences Co. Ltd, Suzhou, P. R. China. [8]International College of Pharmaceutical Innovation, Soochow University, Suzhou, P. R. China. [9]These authors contributed equally: Qiongzhe Ren, Xiaofei Zhao, Lili Zhou. ✉e-mail: zhoufangfang@suda.edu.cn; xucc@suda.edu.cn; zyzhong@suda.edu.cn

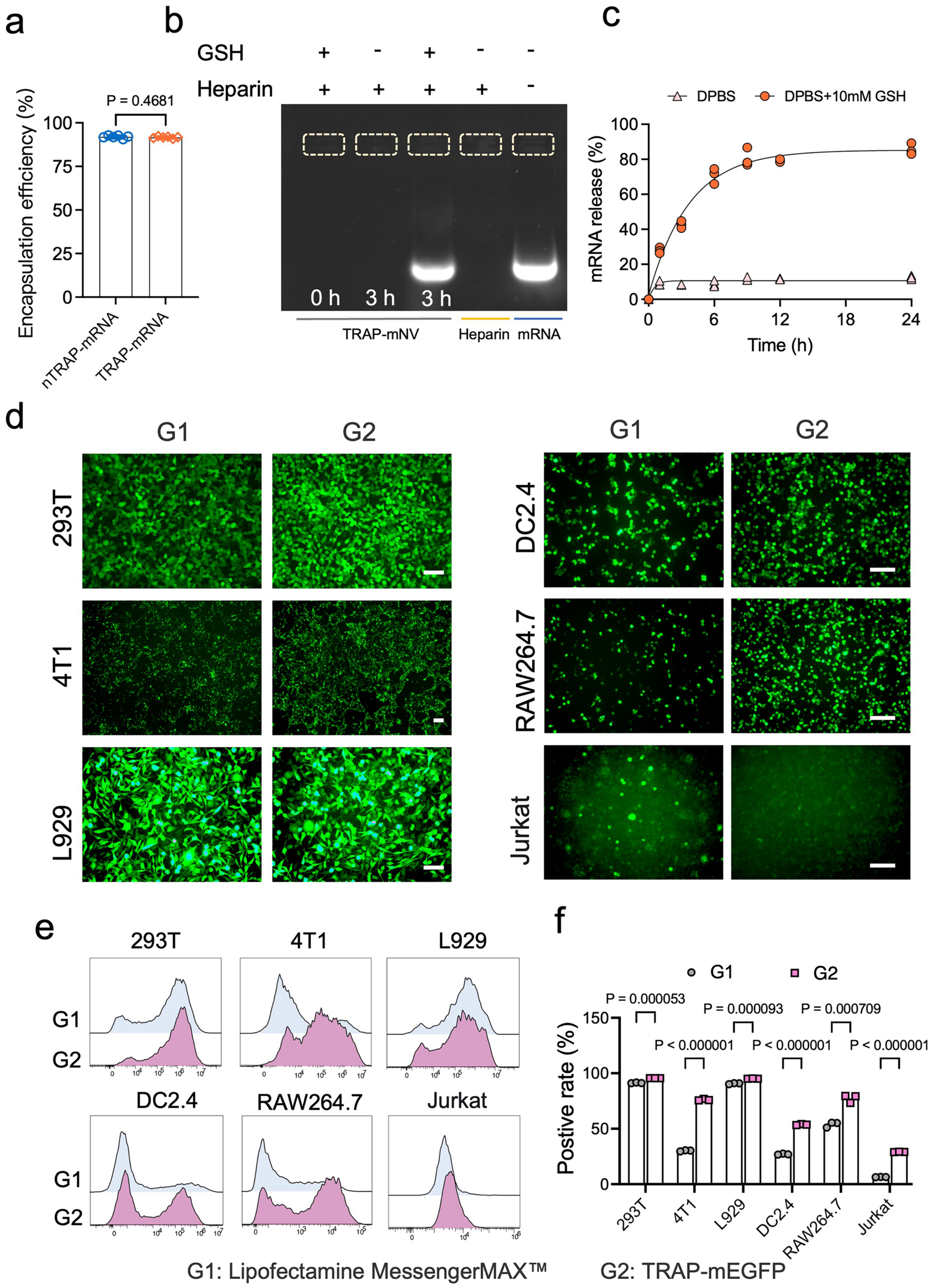

Extended Data Fig. 1 | See next page for caption.

Extended Data Fig. 1 | Physicochemical characterization and transfection performance of TRAP–mRNA complexes. a, Quantification of mRNA encapsulation efficiency by TRAP–mRNA and nTRAP–mRNA formulations (*n* = 6 independent measurements). **b**, Agarose gel electrophoresis showing that mRNA is effectively protected by TRAP. **c**, Time course of mRNA release from TRAP–mRNA complexes in the presence of GSH (0–24 h), as measured by a RibogreenTM assay (*n* = 3 independent measurements). **d**, Representative GFP protein fluorescence imaging of various cells, scale bar: 100 μm. **e**, Representative flow cytometry histograms of mEGFP expression in different cell lines. **f**, Quantification of GFP$^+$ cells determined by flow cytometry (*n* = 3 biological samples). Data in **a**,**c**,**f** are presented as mean values ± s.d. The experiments in **b** and **d** were independently repeated at least three times with similar results. Statistical significance for panel **f** was determined by multiple two-sided unpaired Student's *t*-tests with correction for multiple comparisons, by two-sided unpaired Student's *t*-test for panel **a**. Exact *P* values are provided in the figures where applicable. Source data are provided.

https://doi.org/10.1038/s41551-026-01672-0

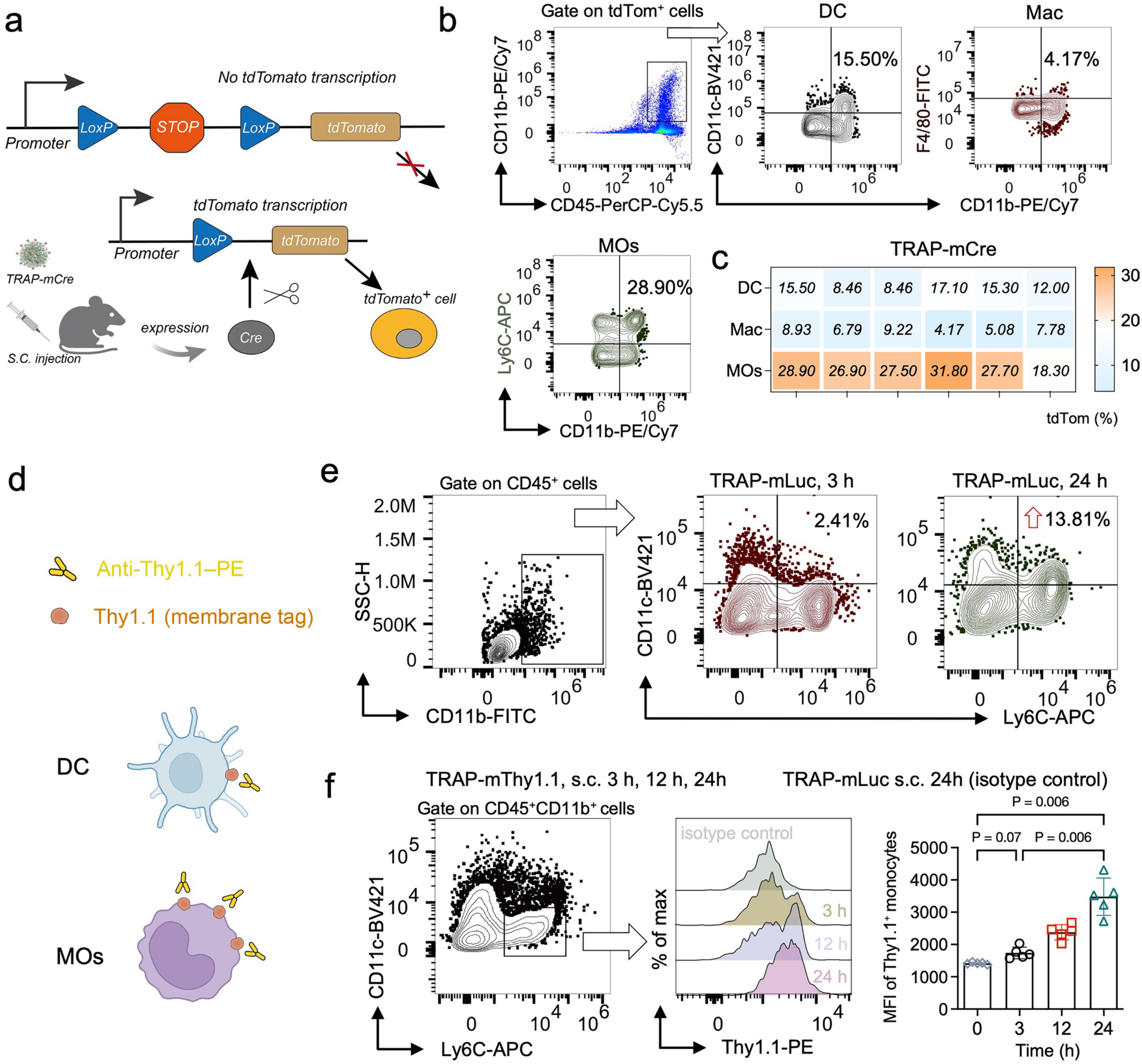

Extended Data Fig. 2 | mRNA translation in lymph nodes following TRAP–mRNA administration. **a**, Schematic illustration of Cre mRNA-mediated tdTomato expression in cells, where TRAP-mCre induces recombination and tdTomato expression through excision of the LoxP-flanked STOP cassette. **b**, Representative flow cytometry plots showing tdTomato$^+$ DCs, Macs, and MOs in inguinal lymph nodes 48 h after subcutaneous injection of TRAP-mCre. **c**, Quantitative summary of Cre mRNA delivery efficiency, shown as the percentage of tdTomato$^+$ cells among each immune-cell subset (*n* = 3 biological samples). **d**, Schematic representation of Thy1.1 (membrane-anchored) reporter expression following TRAP-mediated delivery of Thy1.1 mRNA, used to trace translation events in DCs and MOs within lymph nodes. **e**, Representative flow cytometry plots showing the frequency of Ly6C$^+$CD11c$^+$cells in inguinal lymph nodes at 3 h and 24 h after subcutaneous injection of TRAP–mLuc nanoparticles. **f**, Representative histogram overlays depicting Thy1.1 expression in Ly6C$^+$CD11c$^-$ monocytes at 3 h, 12 h, and 24 h post-injection of TRAP–mThy1.1, and TRAP–mLuc treated mice served as isotype controls. Quantification of the MFI of Thy1.1$^+$ MOs (*n* = 5 biological samples). Data in **c** and **f** are presented as mean values ± s.d. Statistical significance in **f** was determined by ordinary one-way ANOVA (two-sided). Source data are provided.

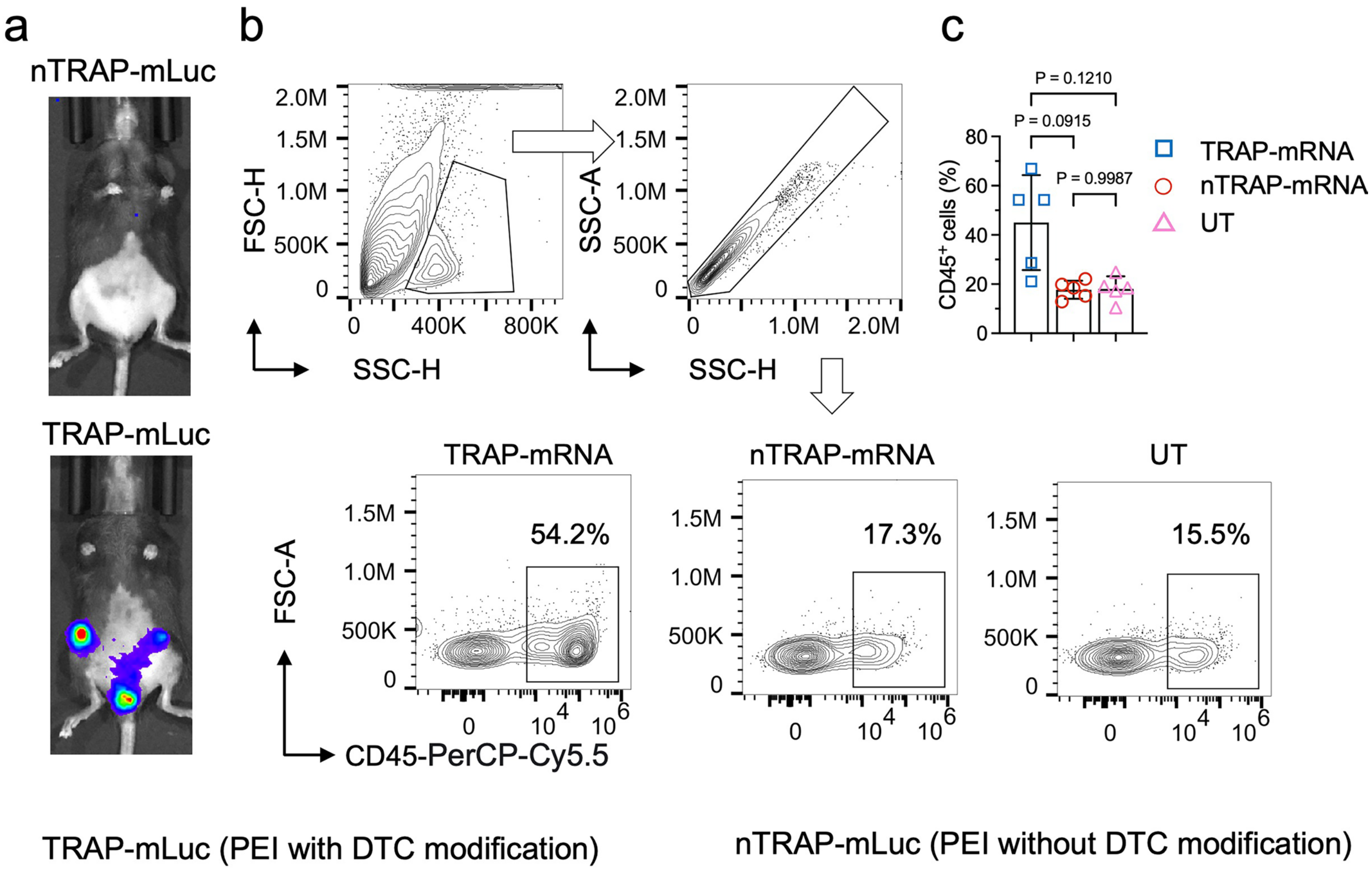

Extended Data Fig. 3 | TRAP enhances local immune-cell recruitment following subcutaneous administration. **a**, Representative IVIS bioluminescence images showing luciferase expression after subcutaneous administration of TRAP–mLuc or non-targeted nTRAP–mLuc. **b**, Flow cytometry analysis of CD45$^+$ immune-cell infiltration at the injection site in untreated (UT), nTRAP–mLuc, and TRAP–mLuc-treated mice. **c**, Quantification of CD45$^+$ immune-cell proportions across groups (*n* = 5 biological samples). Data in **c** is presented as mean values ± s.d. Statistical significance in **c** was determined by ordinary one-way ANOVA (two-sided). Source data are provided.

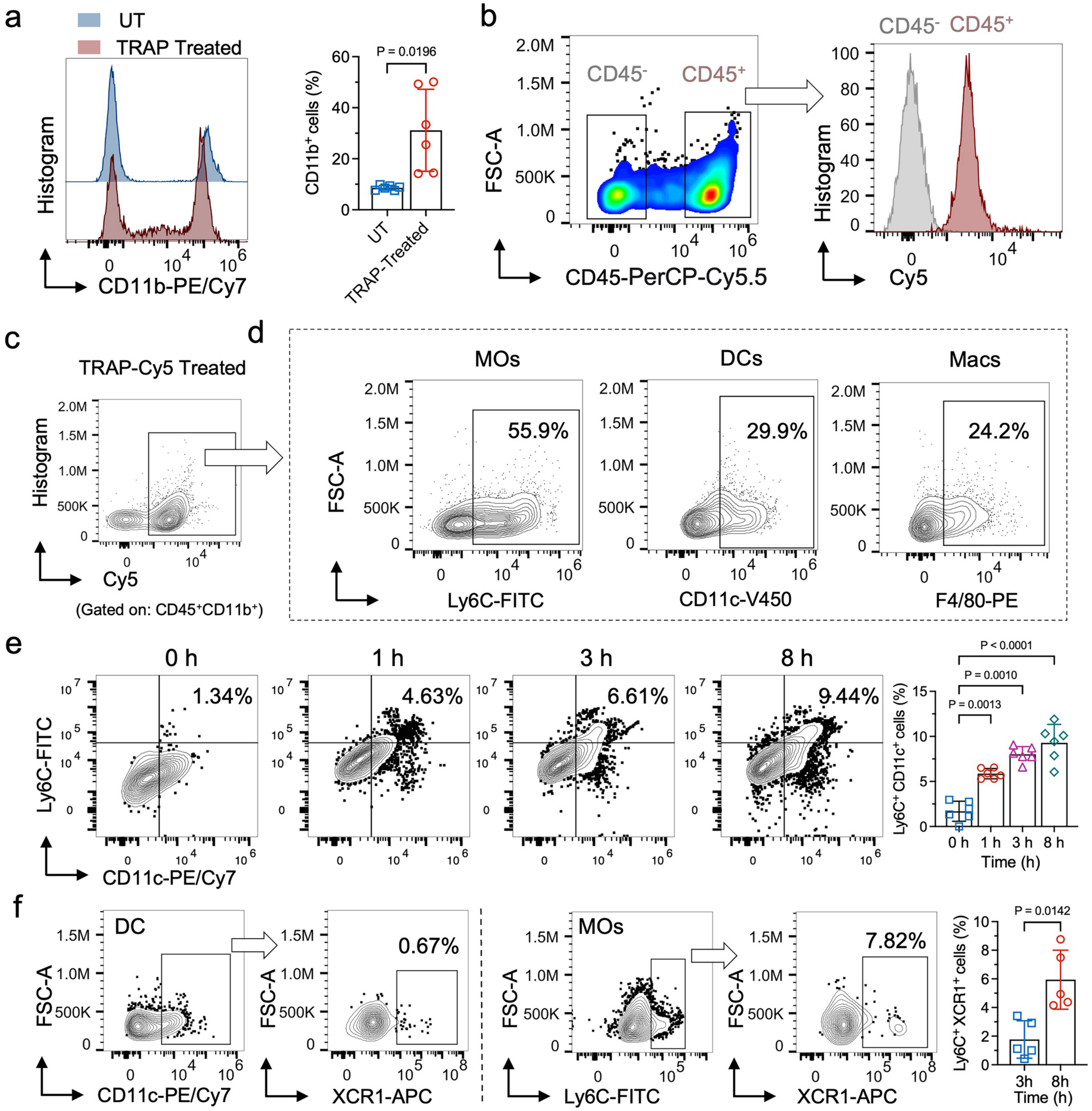

Extended Data Fig. 4 | TRAP–mRNA uptake and monocyte differentiation dynamics at the injection site. a, Subcutaneous administration of TRAP–mRNA leads to increased recruitment of CD11b$^+$ myeloid cells at the injection site, as shown by representative flow cytometry histograms and quantification (*n* = 6 biological samples). **b**, Comparative analysis of TRAP–mRNA (Cy5-labelled) uptake between immune (CD45$^+$) and non-immune (CD45$^-$) cell populations at the injection site, shown by representative dot plots and fluorescence intensity histograms. **c**, Representative flow cytometry plot showing Cy5 signal in CD45$^+$CD11b$^+$ myeloid cells following subcutaneous injection of TRAP-Cy5-mRNA. **d**, Among Cy5$^+$ myeloid cells, monocytes (Ly6C$^+$), dendritic cells (CD11c$^+$), and macrophages (F4/80$^+$) account. **e**, Time-course analysis of monocyte differentiation at the injection site, as evidenced by the progressive increase in CD11c expression on Ly6C$^+$ monocytes from 0 h to 8 h post-injection and quantification of Ly6C$^+$CD11c$^+$ double-positive cells over time (*n* = 5 biological samples). **f**, Temporal expression of XCR1 in Ly6C$^+$ monocytes at the injection site, as assessed by flow cytometry at 3-, and 8-h post-injection, with representative plots and quantification (*n* = 5 biological samples). Data in **a**, **e** and **f** are presented as mean values ± s.d. Statistical significance was determined by one-way ANOVA (two-sided) for panels **e** and **f**, by two-sided unpaired Student's *t*-test for panel **a**. Source data are provided.

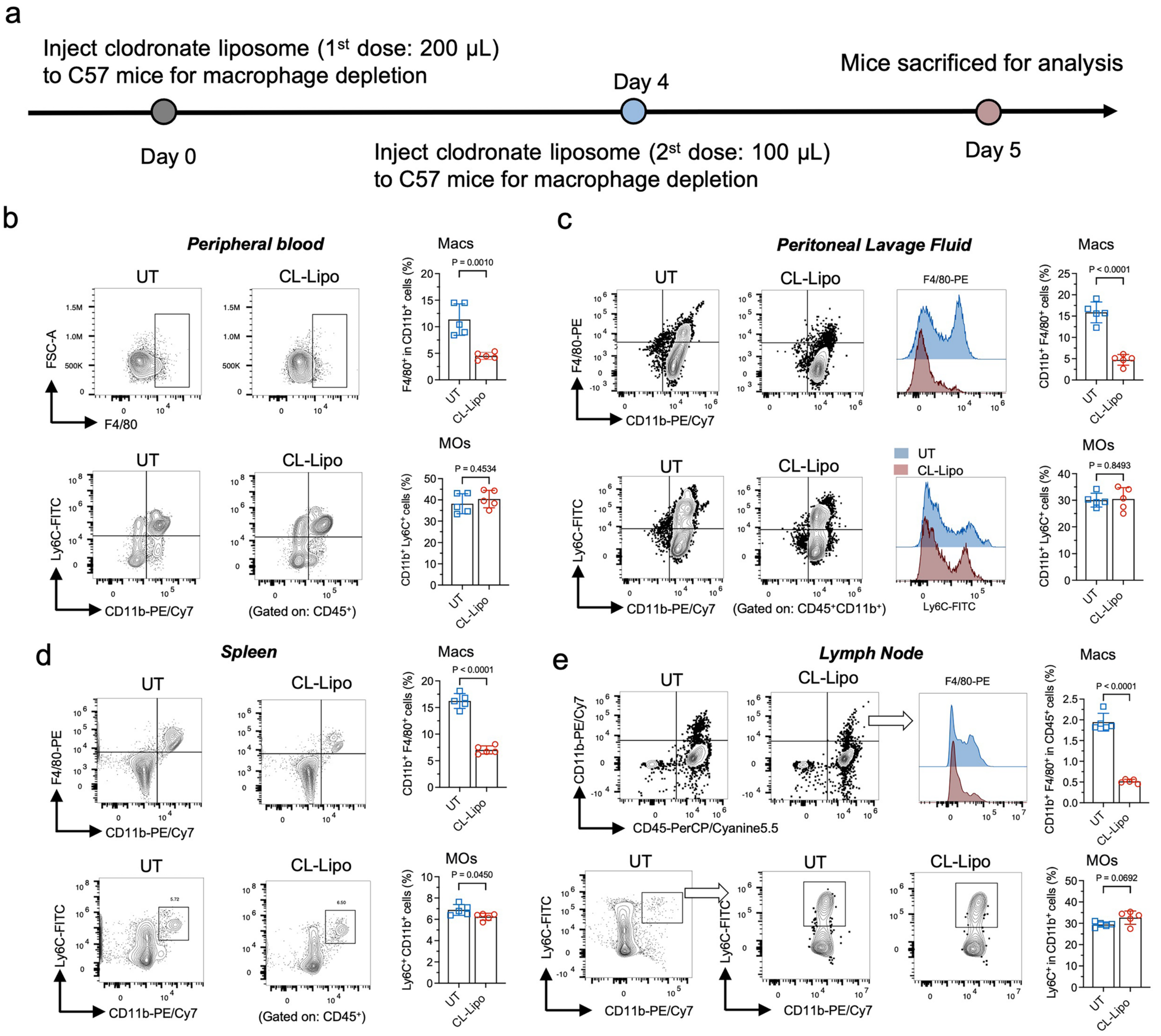

Extended Data Fig. 5 | Systemic depletion of macrophages by clodronate liposome administration. a, Schematic illustration of the in vivo macrophage depletion protocol. C57BL/6 mice were intraperitoneally injected with clodronate liposomes (CL-Lipo; 200 μl on day 0 and 100 μl on day 4), and tissues were harvested on day 5 for analysis. **b**–**e**, Representative flow cytometry plots and quantification of macrophages (F4/80$^+$) and monocytes (Ly6C$^+$) in (**b**) peripheral blood, (**c**) peritoneal lavage fluid, (**d**) spleens and (**e**) lymph nodes from untreated (UT) and CL-Lipo–treated mice (*n* = 5 mice per group). Data are presented as mean values ± s.d. Statistical significance was determined by a two-sided unpaired Student's *t*-test. Exact *P* values are provided in the figure where applicable. Source data are provided.

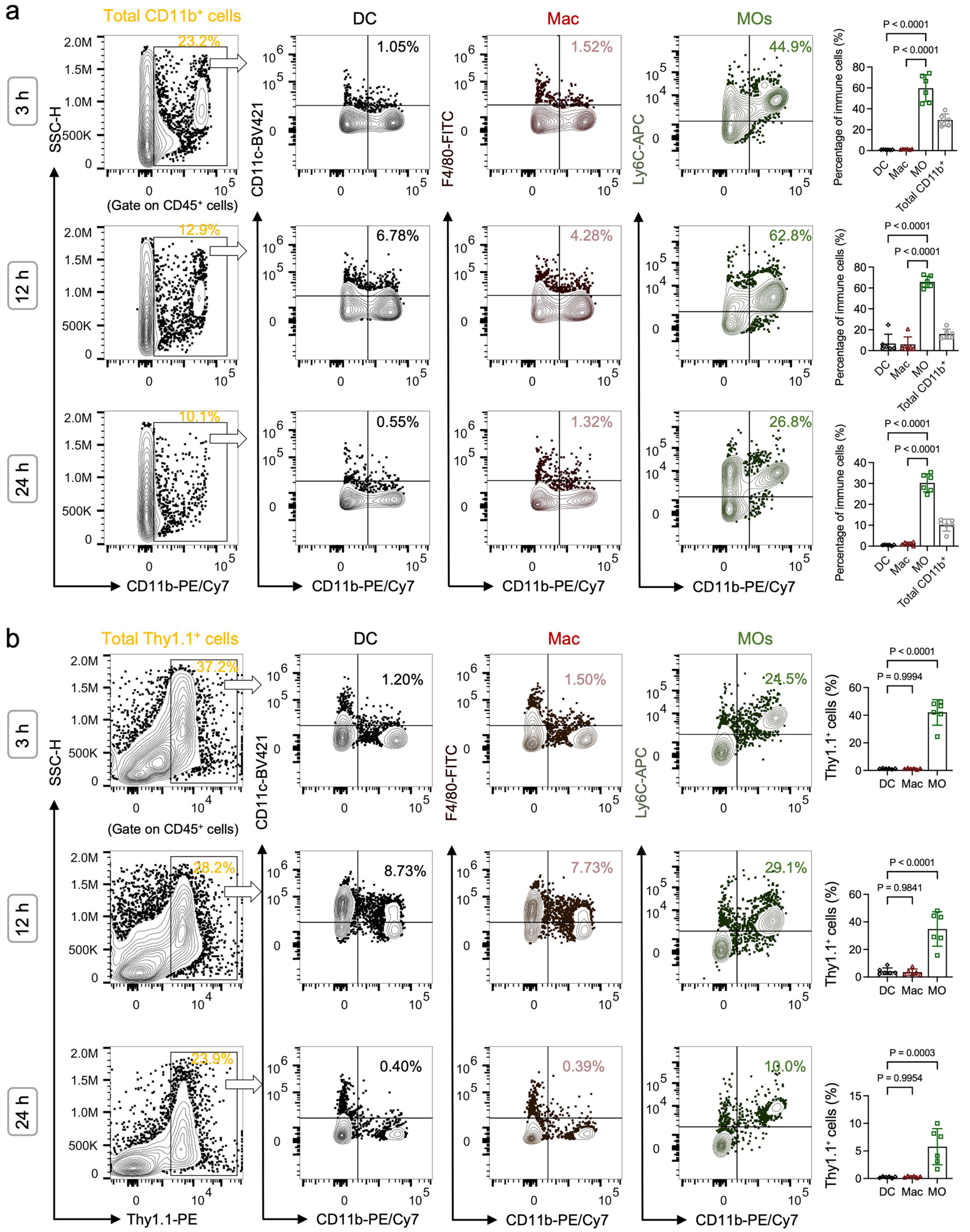

Extended Data Fig. 6 | See next page for caption.

Extended Data Fig. 6 | Tracking in situ recruitment and TRAP-Thy1.1 mRNA expression in myeloid cells at the injection site. a, Flow cytometry analysis of $CD11b^+$ cells at 3 h, 12 h, and 24 h following subcutaneous injection of TRAP–mThy1.1. Representative gating on $CD11b^+$ cells is shown, with quantification of DCs, Macs, and MOs among the recruited $CD11b^+$ population at the injection site over time (*n* = 6 biological samples). **b**, Representative flow cytometry plots showing Thy1.1$^+$ cells at 3 h, 12 h, and 24 h post-injection. Quantification of DCs, Macs, and MOs within the Thy1.1$^+$ population reveals the distribution of translation-active myeloid subsets at the injection site (*n* = 6 biological samples). Thy1.1 encodes a membrane-anchored reporter protein, enabling detection of mRNA translation following TRAP-mediated delivery. Data in **a** and **b** are presented as mean values ± s.d. Statistical significance was determined by one-way ANOVA (two-sided). Exact *P* values are provided in the figure where applicable. Source data are provided.

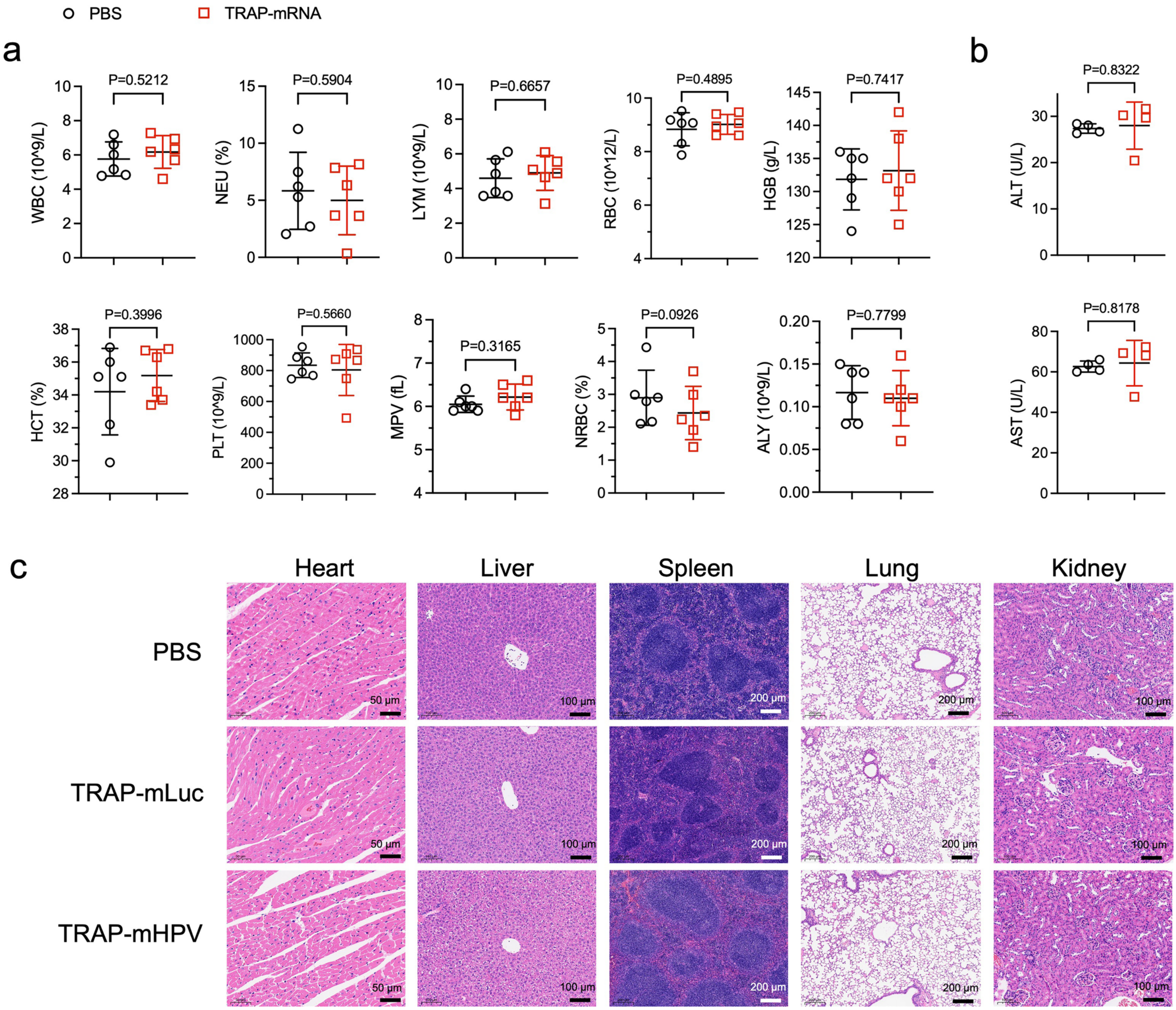

Extended Data Fig. 7 | Comprehensive safety evaluation of TRAP–mRNA vaccination. a, Complete blood count (CBC) parameters were analysed 24 h post-injection in mice receiving subcutaneous administration of TRAP–mRNA nanoparticles (3 μg mRNA, N/P = 10) or PBS (*n* = 6 mice per group), including WBC, NEU, LYM, RBC, HGB, HCT, PLT, MPV, NRBC, and ALY. No significant differences were observed between groups. **b**, Serum biochemical indicators of liver function (ALT and AST) measured 24 h post-injection (*n* = 4 mice per group) showed no evidence of hepatotoxicity in TRAP–mRNA-treated mice compared with PBS controls. **c**, Representative hematoxylin and eosin (H&E)-stained sections of major organs (heart, liver, spleen, lung, and kidney) collected 24 h post-injection from mice treated with TRAP–mLuc (control) or TRAP–mHPV revealed no apparent histopathological abnormalities, indicating minimal off-target tissue toxicity. Data are presented as mean ± s.d. Statistical significance was assessed using a two-tailed unpaired Student's *t*-test. Exact *P* values are provided in the figure where applicable. Source data are provided.

nature portfolio

Corresponding author(s): congcong Xu

Last updated by author(s): Feb 13, 2026

Reporting Summary

Nature Portfolio wishes to improve the reproducibility of the work that we publish. This form provides structure for consistency and transparency in reporting. For further information on Nature Portfolio policies, see our Editorial Policies and the Editorial Policy Checklist.

Statistics

For all statistical analyses, confirm that the following items are present in the figure legend, table legend, main text, or Methods section.

n/a	Confirmed	
☐	☒	The exact sample size (*n*) for each experimental group/condition, given as a discrete number and unit of measurement
☐	☒	A statement on whether measurements were taken from distinct samples or whether the same sample was measured repeatedly
☐	☒	The statistical test(s) used AND whether they are one- or two-sided *Only common tests should be described solely by name; describe more complex techniques in the Methods section.*
☒	☐	A description of all covariates tested
☐	☒	A description of any assumptions or corrections, such as tests of normality and adjustment for multiple comparisons
☐	☒	A full description of the statistical parameters including central tendency (e.g. means) or other basic estimates (e.g. regression coefficient) AND variation (e.g. standard deviation) or associated estimates of uncertainty (e.g. confidence intervals)
☐	☒	For null hypothesis testing, the test statistic (e.g. *F*, *t*, *r*) with confidence intervals, effect sizes, degrees of freedom and *P* value noted *Give P values as exact values whenever suitable.*
☒	☐	For Bayesian analysis, information on the choice of priors and Markov chain Monte Carlo settings
☒	☐	For hierarchical and complex designs, identification of the appropriate level for tests and full reporting of outcomes
☐	☒	Estimates of effect sizes (e.g. Cohen's *d*, Pearson's *r*), indicating how they were calculated

Our web collection on statistics for biologists contains articles on many of the points above.

Software and code

Policy information about availability of computer code

Data collection	Coarse-grained molecular dynamics simulations (CGMD): GROMACS 2023.2 package; Size and zeta potential data: Malvern Zetasizer Nano ZS;Uv data: UH5300 Hitachi; TEM images: Transmission Electron Microscope HT7700 120kV; Confocal laser scanning microscopy (CLSM) images: Abberior Instrument Expert Line STED super-resolution microscope, High Intelligent and Sensitive SIM; Flow Cytometer: BD FACVERSE; BECKMAN CYTOPLEX; Animal Imaging data: PerkinElmer IVIS Spectrum;
Data analysis	Visual Molecular Dynsmics (VMD) 1.9.4; UCSF ChimeraX 1.9; Zetasizer version 7.13, Malvern Panalytical; Image J Fiji 1.53c; MestReNova x64 V14.2.0; PK Living Image software version 4.2; ImarisViewer 10.2.0; IVM Studio V23.12.040; STEDYCON Gallery; FlowJo v10 10.7.1; Graphpad Prism v. 10.0; Adobe Illustrator 2023.

For manuscripts utilizing custom algorithms or software that are central to the research but not yet described in published literature, software must be made available to editors and reviewers. We strongly encourage code deposition in a community repository (e.g. GitHub). See the Nature Portfolio guidelines for submitting code & software for further information.

Data

Policy information about availability of data

All manuscripts must include a data availability statement. This statement should provide the following information, where applicable:

- Accession codes, unique identifiers, or web links for publicly available datasets
- A description of any restrictions on data availability
- For clinical datasets or third party data, please ensure that the statement adheres to our policy

Raw data are available upon request. Other data are presented in the main text and supplementary information.

Research involving human participants, their data, or biological material

Policy information about studies with human participants or human data. See also policy information about sex, gender (identity/presentation), and sexual orientation and race, ethnicity and racism.

Reporting on sex and gender	N/A
Reporting on race, ethnicity, or other socially relevant groupings	N/A
Population characteristics	N/A
Recruitment	N/A
Ethics oversight	N/A

Note that full information on the approval of the study protocol must also be provided in the manuscript.

Field-specific reporting

Please select the one below that is the best fit for your research. If you are not sure, read the appropriate sections before making your selection.

☒ Life sciences ☐ Behavioural & social sciences ☐ Ecological, evolutionary & environmental sciences

For a reference copy of the document with all sections, see nature.com/documents/nr-reporting-summary-flat.pdf

Life sciences study design

All studies must disclose on these points even when the disclosure is negative.

Sample size	To ensure statistical significance, all in vitro experiments described in this paper were performed with n > 3. A minimum of 3 independent repeats was required to evaluate statistical significance; For in vivo mRNA distribution and expression analysis in mice, a sample size of n = 3 was chosen based on standard practices for preliminary biological studies. Based on our experience with the B16F10 murine melanoma and TC-1 model, we used group sizes of 5 animals for the tumor growth experiments. This group size provides enough power to detect statistically significant differences in survival rate and/or tumor size.
Data exclusions	No data were excluded.
Replication	Cell experiments were performed with 3 biological replicates unless otherwise stated, the sample sizes are indicated in the figure legends. We have used C57BL/6 mice to determine tissue specific mRNA delivery in the organ. Each experiment was performed with 3 biological replicates. Numbers of replicated events were detailed in the relevant figure legends. Experiments were repeated at least three times and experimental findings were reproducible.
Randomization	All experimental samples or models were allocated randomly to each treatment group.
Blinding	In histological and immunohistochemical assessments, the tissue section analysis was performed by an senior investigator who was unaware of treatment allocation. ForI other experiments, data collection and analysis were not performed blind to the conditions of the experiments, as the data were aquired with the same equipment, which did not need grading by subjective judgment.

Reporting for specific materials, systems and methods

We require information from authors about some types of materials, experimental systems and methods used in many studies. Here, indicate whether each material, system or method listed is relevant to your study. If you are not sure if a list item applies to your research, read the appropriate section before selecting a response.

Materials & experimental systems

n/a	Involved in the study	
☐	☒	Antibodies
☐	☒	Eukaryotic cell lines
☒	☐	Palaeontology and archaeology
☐	☒	Animals and other organisms
☒	☐	Clinical data
☒	☐	Dual use research of concern
☒	☐	Plants

Methods

n/a	Involved in the study	
☒	☐	ChIP-seq
☐	☒	Flow cytometry
☒	☐	MRI-based neuroimaging

Antibodies

Antibodies used

All the antibodies were diluted and used following the supplier's protocols.
Flow cytometry:
anti-CD11b (clone M1/70, BioLegend, 101215, 1:200),
anti-CD11b (clone M1/70, BioLegend, 101211, 1:200),
anti-CD11b (clone M1/70, BioLegend, 101216, 1:200),
anti-CD11c (clone N418, BioLegend, 117329, 1:200),
anti-CD11c (clone N418, BioLegend, 117317, 1:200),
anti-CD11c (clone N418, BioLegend, 117305, 1:200),
anti-CD11c (clone N418, BioLegend, 117310, 1:200),
anti-Ly6C (clone HK1.4, BioLegend, 128005, 1:200),
anti-Ly6C (clone HK1.4, BioLegend, 128016, 1:200),
anti-64 (clone S18017D, BioLegend, 161003, 1:200),
anti-CD45 (clone 30-F11, BioLegend, 103112, 1:200),
anti-CD45 (clone 30-F11, BioLegend, 103132, 1:200),
anti-86 (clone A17199A, BioLegend, 159204, 1:200),
anti-80 (clone 16-10A1, BioLegend, 104706, 1:200),
anti- H-2Kd/H-2Dd (clone 34-1-2S, BioLegend, 114715, 1:200),
anti-CD3 (clone 17A2, BioLegend, 100204, 1:300)
anti-CD3 (clone 17A2, BioLegend, 100236, 1:300)
anti-CD8a (clone 53-6.7, BioLegend, 100706, 1:300)
anti-CD8a (clone 53-6.7, BioLegend, 100708, 1:300)
anti-CD4 (clone GK1.5, BioLegend, 100408, 1:200)
anti-F4/80(clone BM8, BioLegend, 123115, 1:200)
anti-F4/80(clone W20065B, BioLegend, 111603, 1:200)
anti-XCR1(clone ZET, BioLegend, 148206, 1:200)
anti-CD90.1(clone S20007C, BioLegend, 109006, 1:200)
anti-IFN-γ (clone XMG1.2, BioLegend, 505810, 1:200)
anti-CD16/32 (clone 93, BioLegend, 101302, 1:30)
anti-NK1.1 (clone PK136, BioLegend, 108727, 1:200),
anti-zombie NIR (BioLegend, 423105 , 1:10000),
anti-H-2Kb OVA Tetramer-SIINFEKL (MBL, TS-5001-1C , 1:200),
anti-CD4 (clone GK1.5, BioLegend, 100408, 1:300),
anti-CD25 (clone PC61, BioLegend, 102016, 1:300),
anti-CD69 (clone H1.2F3, BioLegend, 104511 &104512, 1:300),
anti-CD62L (clone MEL-14, BioLegend, 161204, 1:300),
anti-CD44 (clone IM7, BioLegend, 103031, 1:300),
Block antibody:
inVivo MAb anti-mouse L-Selection (clone Mel-14, Bio X Cell, 794822J1, 1:200)
inVivo MAb anti-mouse PSGL-1 (clone 4RA10, Bio X Cell, 808722M1, 1:200)

Validation

The antibodies used in this manuscript were bought from commercial sources and validated by the supplier.
According to statements on the manufacturers websites, each antibody used in this study was validated for flow cytometry applications: anti-CD11b (https://www.biolegend.com/en-gb/products/pe-cyanine7-anti-mouse-human-cd11b-antibody-1921), anti-CD11c (https://www.biolegend.com/en-gb/products/fitc-anti-mouse-cd11c-antibody-1815), CD11c (https://www.biolegend.com/en-gb/products/apc-anti-mouse-cd11c-antibody-1813), anti-Ly6C (https://www.biolegend.com/en-gb/products/fitc-anti-mouse-ly-6c-antibody-4896), anti-64 (https://www.biolegend.com/en-gb/products/pe-anti-mouse-cd64-fcγri-antibody-21518), anti-CD45 (https://www.biolegend.com/en-gb/products/apc-anti-mouse-cd45-antibody-97), anti-86 (https://www.biolegend.com/en-gb/products/pe-anti-mouse-cd86-antibody-18945), anti-80 (https://www.biolegend.com/en-gb/products/fitc-anti-mouse-cd80-antibody-41), anti-H-2Kd/H-2Dd (https://www.biolegend.com/en-gb/products/percp-cyanine5-5-anti-mouse-h-2kd-h-2dd-antibody-15820), anti-CD3 (https://www.biolegend.com/en-gb/products/fitc-anti-mouse-cd3-antibody-45), anti-CD3 (https://www.biolegend.com/en-gb/products/apc-anti-mouse-cd3-antibody-8055),anti-CD8a (https://www.biolegend.com/en-gb/products/fitc-anti-mouse-cd8a-antibody-153), anti-CD8a (https://www.biolegend.com/en-gb/products/pe-anti-mouse-cd8a-antibody-155),anti-IFN-γ (https://www.biolegend.com/en-gb/products/apc-anti-mouse-ifn-gamma-antibody-993), anti-NK1.1 (https://www.biolegend.com/en-gb/products/percp-cyanine5-5-anti-mouse-nk-11-antibody-4289), anti-Live/Dead (https://www.biolegend.com/en-gb/products/zombie-nir-fixable-viability-kit-8657), anti-H-2Kb OVA Tetramer-SIINFEKL (https://www.mblbio.com/bio/g/dtl/T/?pcd=TS-5001-1C), anti-CD4 (https://www.biolegend.com/en-gb/products/pe-anti-mouse-cd4-antibody-250), anti-CD25 (https://www.biolegend.com/en-gb/products/pe-cyanine7-anti-mouse-cd25-antibody-1929), anti-CD62L (https://www.biolegend.com/en-gb/products/pe-anti-mouse-cd62l-antibody-19844), anti-CD44 (https://www.biolegend.com/en-gb/products/percp-cyanine5-5-anti-mouse-human-cd44-

antibody-5605).
As stated on manufacturers/suppliers websites, the following antibodies have been validated for reactivity in mouse: inVivo MAb anti-mouse L-Selection (https://bioxcell.com/invivomab-anti-mouse-l-selectin-cd62l-be0021), inVivo MAb anti-mouse PSGL-1 (https://bioxcell.com/invivomab-anti-mouse-psgl-1-cd162-be0186 queryID=dd2d1ee524b84de735e598ecacc0521a&objectID=30634&indexName=bioxcell_live_default_products).
anti-CD90.1(Https://www.biolegend.com/en-gb/products/pe-anti-mouse-cd90-1-thy1-1-antibody-23901)
anti-XCR1(https://www.biolegend.com/en-gb/products/apc-anti-mouse-rat-xcr1-antibody-10222)

Eukaryotic cell lines

Policy information about cell lines and Sex and Gender in Research

Cell line source(s)	Multiple mouse tumor cell line (LLC, 4T1, B16F10, B16F10-OVA, B16F10-LUC), mouse derived cell lines (DC2.4, RAW264.7) and human cells (L929) were used for in vivo and in vitro experiments. All cell lines were purchased from the Cell Bank of the Chinese Academy of Sciences (Shanghai, China). BMDCs were induced from bone marrow cells collected from the tibia and femur of C57BL/6 mice.
Authentication	The cell lines were not further authenticated after receiving. In all related studies, cell lines with a low passage number were used.
Mycoplasma contamination	The cell lines were not tested for mycoplasma contamination.
Commonly misidentified lines (See ICLAC register)	The study did not involve commonly misidentified cell lines.

Animals and other research organisms

Policy information about studies involving animals; ARRIVE guidelines recommended for reporting animal research, and Sex and Gender in Research

Laboratory animals	Female C57BL/6 mice (6–8 weeks old, approximately 20 g) were obtained from SLAC Laboratory Animal Co., Ltd., and female Ai9 mice (6–8 weeks old, approximately 20 g) were purchased from Suzhou Abogen Biosciences. All animals were maintained under SPF conditions at Soochow University, with ad libitum access to food and water. Mice were housed in climate-controlled rooms under a 12 h light/dark cycle with 40–70% relative humidity and acclimated for at least one week prior to random assignment into experimental groups. All animal procedures were approved by the Ethics Committee of Soochow University (Approval No. SUDA20240716A03) and were conducted in accordance with institutional guidelines for the care and use of laboratory animals.
Wild animals	No wild animals were used in this study.
Reporting on sex	Female mice
Field-collected samples	The study did not involve samples collected from the field.
Ethics oversight	All animal experiments were reviewed and approved by the Ethics Committee of Soochow University (ECSU) (Approval No.SUDA20240716A03), and all protocols of animal studies conformed to the Guide for the Care and Use of Laboratory Animals.

Note that full information on the approval of the study protocol must also be provided in the manuscript.

Plants

Seed stocks	NA
Novel plant genotypes	NA
Authentication	NA

Flow Cytometry

Plots

Confirm that:

☒ The axis labels state the marker and fluorochrome used (e.g. CD4-FITC).

☒ The axis scales are clearly visible. Include numbers along axes only for bottom left plot of group (a 'group' is an analysis of identical markers).

☒ All plots are contour plots with outliers or pseudocolor plots.

☒ A numerical value for number of cells or percentage (with statistics) is provided.

Methodology

Sample preparation	Samples were prepared according toto methods listed in "Flow cytometry " section.
Instrument	Data were acquired on a LSRFortessa (BD Bioscience and BECKMAN CYTOPLEX)
Software	FlowJo v10 10.7.1
Cell population abundance	Cells were not sorted for this study.
Gating strategy	For all experiments, preliminary FSC-A/SSC-A gates were used to exclude debris. Subsequently, SSC-A/SSC-H and FSC-A/FSC-H gates were used to select singlets. FSC-A/FITC-A was used to determine fluorescence. Gating based on GFP-positive was used to determine the in vitro transfection efficiency. Examples of the subsequent plots for the immune cell specificity study are provided in the supplementary material.

☒ Tick this box to confirm that a figure exemplifying the gating strategy is provided in the Supplementary Information.